Retrieving Optical Depth From Shadows In Orbiter Images of Mars

N.M. Hoekzema, M. Garcia-Comas, O.J. Stenzel, E.V. Petrova, N. Thomas, W.J. Markiewicz, K. Gwinner, H.U. Keller, W.A. Delamere

Accepted Manuscript

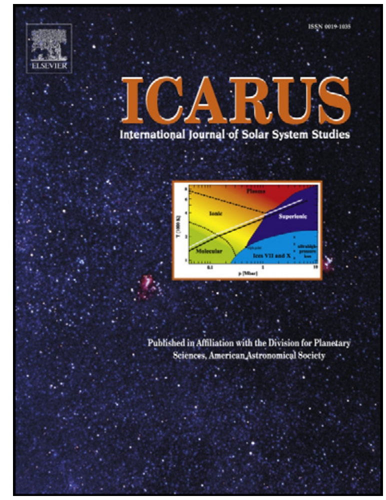

Retrieving Optical Depth From Shadows In Orbiter Images of Mars

N.M. Hoekzema, M. Garcia-Comas, O.J. Stenzel, E.V. Petrova, N. Thomas, W.J. Markiewicz, K. Gwinner, H.U. Keller, W.A. Delamere

PII: S0019-1035(11)00218-1
DOI: 10.1016/j.icarus.2011.06.009
Reference: YICAR 9852

To appear in: *Icarus*

Received Date: 19 October 2010
Revised Date: 3 June 2011
Accepted Date: 7 June 2011

Please cite this article as: Hoekzema, N.M., Garcia-Comas, M., Stenzel, O.J., Petrova, E.V., Thomas, N., Markiewicz, W.J., Gwinner, K., Keller, H.U., Delamere, W.A., Retrieving Optical Depth From Shadows In Orbiter Images of Mars, *Icarus* (2011), doi: 10.1016/j.icarus.2011.06.009

RETRIEVING OPTICAL DEPTH FROM SHADOWS IN ORBITER IMAGES OF MARS

N. M. Hoekzema[1], M. Garcia-Comas[1,2], O. J. Stenzel[1], E. V. Petrova[3], N. Thomas[4], W. J. Markiewicz[1], K. Gwinner[5], H. U. Keller[1,6], W. A. Delamere[7]

[1]Max Planck Institute for Solar System Research, Max Planck Strasse 2, 37191 Katlenburg Lindau, Germany

[2] Instituto de Astrofísica de Andalucía (CSIC), P.O. Box 3004, 18008 Granada, Spain

[3] Space Research Institute RAS, Profsoyuznaya 84/32, Moscow, 117997, Russia

[4]Space Research and Planetology Division, Physikalisches Institut, Sidlerstrasse 5, CH-3012 Bern, Switzerland

[5] DLR, Rutherfordstr. 2, D-12489 Berlin, Germany

[6] IGEP TU Braunschweig, Mendelssohnstr. 3, D-38106 Braunschweig, Germany

[7]Delamere Support Systems, Boulder CO 80304, USA

Corresponding author:

Dr. Nick Hoekzema

Max Planck Institute for Solar System Research

Max Planck Strasse 2

37191 Katlenburg Lindau

Germany

tel [49] 5556 979 438

fax [49] 5556 979 141

hoekzema@mps.mpg.de

[2] maya@iaa.es

[1]stenzel@mps.mpg.de

[3]epetrova@iki.rssi.ru

[4]nicolas.thomas@space.unibe.ch

[5]Klaus.Gwinner@dlr.de

[6]keller@mps.mpg.de

[7] alan@delamere.biz

Abstract

The difference in brightness between shadowed and sunlit regions in space images of Mars is a measure of the optical depth of the atmosphere. The translation of this difference into optical depth is what we name the "shadow method". Our analysis of two HRSC data-sets and a HiRISE data-set indicates that it is possible to estimate the optical depth with the shadow method. In colors between yellow and red the accuracy may be around ± 15%, and in some cases ± 8-10%. In other colors we found larger errors.

We came to these results in two steps. First, we investigated in how far shadow method retrievals are proportional to the true optical depth. To this end we analyzed about 150 locations in Valles Marineris that were imaged by HRSC. Whereas the studied region spans about 8 km in altitude we were able to study the relation between altitude and shadow-method retrievals. Retrievals from five HRSC panchromatic (675 ± 90 nm) stereo images yielded scale-heights with an average of 12.2 ± 0.7 km, which is very close to the expected local pressure scale height. Many studies have shown that the scale-height of optical depth and pressure commonly are similar. This indicates that the shadow method retrievals are on average close to proportional to the optical depth, because otherwise these would probably not yield a correct scale-height. HRSC's red image yielded very similar results, but the blue, green, and NIR images did not.

Next, we compared optical depth measurements by the two MER rovers with shadow method retrievals from orbiter images of the rover exploration sites. Retrievals with the shadow method appear systematically smaller than the rover

measurements; dividing the retrievals by a "correction factor" yields an estimate of the real optical depth. Retrievals from three HRSC panchromatic stereo images of a region near the Spirit rover yielded a correction factor of 0.63 ± 0.09 when the sunlit comparison regions were at varying and more or less arbitrary distances from the shadows and 0.71 ± 0.06 when these were close together. Twenty retrievals from a HiRISE red (650 ± 100 nm) image of the Opportunity exploration site similarly yielded 0.68 ± 0.09. The results from these two case studies suggest that the shadow method has an accuracy of about ± 15% or around ± 8-10% in the best cases.

Keywords: atmosphere, optical-depth, scale height, shadow, MER rover

1. Introduction

The optical depth of the martian atmosphere can be estimated with the so called "shadow method". An estimate with this method follows from the difference between the brightness of a shadow and the brightness of a sunlit comparison region. This paper presents the theory behind a simple version of the shadow method. Moreover, we analyze three data sets to test it. For these tests we use space images of Mars taken with the High Resolution Stereo Camera (HRSC) of the European Mars orbiter Mars Express and taken with the High Resolution Imaging Science Experiment (HiRISE) onboard the Mars Reconnaissance Orbiter. A more elaborate validation study that will use more data sets is in progress and we plan to publish results from this study in the future in a separate paper.

The optical depth of the martian atmosphere in the visible is commonly in the range 0.3-1.0, and is mainly determined by a haze of aerosols. Most martian aerosols are reddish particles of airborne dust (Markiewicz et al. 1999, Tomasko et al. 1999). The aerosol haze invokes important atmospheric effects: it largely determines how much insolation is absorbed in the atmosphere and how much reaches the surface, and what fraction reaches the surface in a direct beam and what fraction reaches it as diffuse illumination from the reddish martian sky. The haze also diminishes the contrast and the spatial resolution of orbiter images and interpretation of such images should consider the atmospheric effects. For quantifying these, one in the first place needs to know the optical depth of the atmosphere. Stenzel et al. (2007 & 2008) show how images of Mars can be corrected for atmospheric effects once the optical depth is known.

Developing the shadow method is in the first place useful because it offers an almost model independent and easy way to estimate the optical depth of the martian atmosphere in the visible from space images. Various standard methods that are often used in Earth remote sensing do not (yet) work well for Mars. E.g., the difference between measured TOA albedos (Top Of Atmosphere albedos) and known surface albedos can yield optical depth estimates in remote sensing of Earth (e.g., http://www-misr.jpl.nasa.gov/software/#Introduction). E.g., Stenzel et al. (2008) have developed similar methods for Mars, but at the moment the accuracy of such methods is less than optimal. For Mars accurate ground truth albedos are not generally available, and at present the calibration of most sensors in orbit around Mars does not facilitate accurate measurements of the TOA albedos. Moreover, such optical depth retrieval algorithms require elaborate aerosol models as an input (e.g., Veefkind 1999). Whereas such models do exist for what probably is the common martian airborne dust (Markiewicz et al. 1999, Tomasko et al. 1999, Johnson et al. 2003, Lemmon et al. 2004), condensation of small amounts of ice onto these dust grains will change the average aerosol properties significantly. Also, such models are not valid for the icy high altitude haze layers that often are important as well.

The optical depth can often be retrieved from good stereo imagery with the so called “stereo method” (Hoekzema et al. 2007, Hoekzema et al. 2010), and this method does not depend on aerosol models. It is a useful tool when studying high quality HRSC images, but other cameras in orbit around Mars, like e.g., HiRISE, do not often provide stereo information with which the stereo method can work properly.

Hence, the shadow method could be a useful tool for measuring optical depths, in particular for images with a very high spatial resolution (better than about a meter per pixel) as offered by HiRISE. In such images the martian surface shows shadows frequently; e.g., behind large boulders and behind cliffs in the rims of small fresh craters. Many HiRISE images are so sharp that such shadows are well resolved, and it seems worthwhile to further develop and test the shadow method for these. However, the shadow method is of more limited use for the lower resolution images of other cameras in orbit around Mars because these do not resolve shadows very often. The Digital Terrain Models (DTMs) derived from HRSC stereo imagery have made it clear that at resolutions of 10 or more meters per pixel almost all slopes on Mars only begin to cast usable shadows when the sun is well below 30° above the horizon. When the sun is below some 10° the shadow method (as presented here) becomes inaccurate because it uses a plane parallel approximation which then loses its validity.

The shadow method was used for the first time by Markiewicz et al. (2005). The concept is simple: under a clear sky there is a large brightness difference between sunlit regions and shadowed ones, but with increasing optical depth of the overlying atmosphere this difference gets smaller. It is proposed here as a measure for the optical depth of the local atmosphere. The conversion of this difference in brightness into an optical depth is what we name the "shadow method". However, it is not trivial at all to do the conversion correctly. For this one needs to know: the albedo, the bidirectional reflection properties of the surface, the local surface topography, the distribution of diffuse illumination from the sky, which part of the sky is visible in the shadow and which part is visible in the sunlit comparison region. Petrova et al. (submitted to Planetary and Space Science) do a serious attempt to solve the equations of radiative transfer and present an elaborate version of the shadow method, which e.g., can also be used to estimate surface albedos. However, it is not always possible to work with their method because it requires detailed aerosol models, surface reflection functions, and accurate Digital Terrain Models (DTMs); i.e., inputs that often are not available.

For this paper we developed a simpler version of the shadow method that only requires more readily available inputs because it makes several rough assumptions. Our intention is to provide a tool that yields indications of the optical depth in an easy way, but is not necessarily very accurate. The shadow method as we present it here should in the first place be seen as a fit that gives an empirical relation between optical depth and the difference in brightness between sunlit and shadowed regions. In Section 5.1 we show that retrievals from images taken in colors between yellow and red yield apparently accurate estimates of the scale-height of optical depth and pressure. That is, if the optical depth and the pressure have a similar scale-height and if its value is known with some accuracy. Below we elaborate on these two assumptions. The accuracy with which the scale-height can be derived from shadow method retrievals obviously indicates in how far these retrievals are proportional to the true optical depth. In Section 5.1 we argue that for colors from yellow to red there is a factor that is approximately independent of optical depth between true optical depth and the results of our shadow method. We name this factor the "correction factor" C. In sections 5.2 and 5.3 we estimate its value by comparing shadow method retrievals from regions near the exploration sites of the two MER rovers with the optical depth measurements by these rovers.

The work described in this paper builds on two assumptions. Firstly, the pressure scale-height of the martian atmosphere can be estimated with an accuracy of a few hundred meters from the Global Circulation Model (GCM) available via http://www-mars.lmd.jussieu.fr/ (Angelats i Coll et al. 2005). Secondly, the scale-heights of pressure and of optical depth are close to equal in the lower atmosphere of Mars. We now elaborate on this second assumption.

Many papers indicate that airborne dust in Mars' atmosphere indeed usually has a scale-height that is very similar to the pressure scale height. Jaquin et al. (1986) used limb scans from the Viking orbiters. The authors observed discrete, optically thin, detached haze layers between 30 and 90 km elevation that may have consisted of water ice. Below about 50 km they observed a continuous, reddish haze that extended all the way to the surface, while the color suggests that it was mostly airborne dust. In the 30 to 45 km altitude range the scale height was typically 5 to 7 km, which is close to the expected pressure scale height at that altitude. The authors can not offer much useful information on the lowest 10 to 15 kilometers of the atmosphere, since these regions are optically thick, and thus featureless, when viewed from the limb.

Kahn et al. (1981) analyzed the changing sky brightness during the martian twilight as observed by the Viking landers. They concluded that the dust is exponentially distributed in the lowest 30 km, with a scale-height close to that of the atmosphere. The spectral distribution hinted that the particles low in the atmosphere differ from those higher up. The Pathfinder mission yielded new data and Thomas et al. (1999) used egress observations of Phobos. Their data suggest a scale-height of optical depth in the range 10 to 15 km, which is similar to the expected pressure scale-height.

Chassefiere et al. (1995) used observations from various instruments onboard the Phobos 2 mission to study dust in the lower atmosphere of Mars. They determined that the average particle size of airborne dust is probably in the range 1-2 μm. Furthermore they found similar scale-heights for the dust and pressure of 8-9 km above Tharsis.

From 2004, measurements around $\lambda = 9\mu m$ by the Planetary Fourier Spectrometer of Mars Express began yielding estimates of the opacity scale-height. For a very low region, the Hellas basin, Grassi et al. (2007) gives several values between 8 km and 12 km with errors of 2 or 3 km that are all compatible with the pressure scale height. Over very high surface, the flanks of several of the big volcanoes, Zasova et al. (2005) similarly measured a value close to the expected value of the pressure scale-height for these regions around noon: 11.5 ± 0.5 km.

Lemmon et al. (2004) used observations of the setting Sun by the Spirit rover in Gusev crater to derive a local opacity scale height. They found 11.6 ± 0.6 km, while they mention a local pressure scale height at that moment of 11.1 km.

HRSC has been mapping Mars in stereo and in color since January 2004. Its images and the Digital Terrain Models (DTMs) that are derived from these offer new ways to measure the scale-height of optical depth in the martian atmosphere; that is: if one can estimate the optical depth above the martian surface with e.g., the shadow method that we are testing here, or with the stereo method. By estimating optical depth above surfaces that differ in altitude the relation between optical depth and elevation of the surface becomes visible, and a scale-height can be calculated.

Hoekzema et al. (2007) used the stereo method to measure the scale-height of optical depth on the flanks of the volcano Pavonis Mons from HRSC stereo images, which yielded a value of 10.8 km +0.9/-0.8 km. Hoekzema et al. (2010) used the stereo method to measure it on the slopes of Valles Marineris from HRSC observations taken during orbit 471 of MEX and here they find 14.0 -1.1/+1.3 km. Note that the Valles is at considerably lower altitude and thus is warmer and thus should be expected to have a larger scale-height than the Pavonis Mons region. In both cases the estimated scale height of optical depth is very close to the local pressure scale height as expected from the consulted GCM.

To test how accurately the scale-height can be derived from retrievals with the shadow method we analyzed images of Valles Marineris because this region displays huge altitude differences (over 8 km in the data set used here) thus allowing measurements of optical depth as a function of altitude. We choose HRSC stereo images because for these there is a DTM available. Whereas the stereo images of HRSC are taken at differing phase angles, the spread between the results from these images depends on the accuracy of the Lambertian approximation that we use in our method. We choose images from Mars Express orbit 1944 because these show clear shadows and do not show any obvious dust storm activity, and neither any of the bright hazes, that quite often cover the floor of the Valles (see e.g., Inada et al., 2008). We checked for the presence of bright clouds, which could easily inhibit accurate retrievals, by studying the blue and green images of this data-set, and did not find any.

Section 2 offers information about HRSC and HiRISE. Section 3 gives basic theory behind our version of the shadow method. Section 4 offers details on the HRSC and HiRISE images that we used for our analysis. We offer results and some discussion in Section 5 and conclusions in Section 6.

2. Instruments

2.1. HRSC

High Resolution Stereo Cameras (HRSCs) have been developed and built by DLR (Deutsches Zentrum für Luft- und Raumfahrt) in Berlin (Neukum et al. 2004, Jaumann et al. 2007). These are multiple line pushbroom scanning instruments; nine CCD line detectors are mounted inside one optical system. As the MEX spacecraft moves along its orbit, its HRSC acquires superimposed image tracks. The line detectors, often referred to as sensors or channels, have 5184 pixels each. Four of them are equipped with band-pass color filters: blue (440 ± 45 nm), green (530 ± 45 nm), red (750 ± 20 nm), and NIR (near infra red, 970 ± 45 nm). The other five are panchromatic (675 ± 90 nm) and are used for stereo imaging. These stereo channels are named S1, P1, nadir (or ND), P2, and S2. During the observations used for this paper S2 was forward and S1 was backward looking, but for many orbits it is the other way around. The panchromatic stereo channels observe at -18.9º, -12.8º, 0º, 12.8º, and 18.9º as measured from the nadir channel. The color detectors do not observe in the same direction as the nadir one, but under angles of: -15.9º for NIR, -3.3º for green, 3.3º for blue, and 15.9º for red. For the analysis of Valles Marineris we used all nine images, for the analysis of Gusev we only used S1, ND, and S2. The image that we call the 'nadir image' has its name because it was taken by the panchromatic stereo sensor called 'nadir' or 'nadir channel', but the sensor is almost never exactly nadir looking. There almost always is a small offset, during the orbits used here it was never more than 3º-4º, but sometimes it is large (e.g., during limb sounding). Also, images of the other channels are rarely observed with surface emission angles that are equal to their angle with the nadir channel, whereas there are almost always differences because of the influences of the spacecraft orientation, of the swath of the camera of ±6°, and of the curvature of the planet. E.g., the average emission angle for the outer stereo images during their imaging of Valles Marineris is not 18.9º, but 21.6º for S1 and 22.4º for S2.

The spatial resolution of the HRSC on MEX from the nominal periapsis altitude of 300 km above Mars is 12 meter per pixel with an image swath of 62 km (11.9º), and a minimum swath length of about 300 km, otherwise the overlap between e.g., the forward and the backward tracks would be quite small. All tracks are always observed at time intervals of less than a few minutes, which is the time it takes MEX to travel a few hundred kilometers at an orbital velocity of roughly 4 km/s close to periapsis. Therefore, only small temporal variations will exist between them. At true anomalies of ± 20º the spatial resolution is 15 meter per pixel.

2.2. HiRISE

NASA's Mars Reconnaissance Orbiter (MRO) was launched on August 12, 2005. Mars Orbit Insertion occurred on March 10, 2006 and the first in-orbit data was received shortly afterwards. The High Resolution Imaging Science Experiment (HiRISE) is flying onboard the orbiter. It consists of an off-axis telescope with a 0.5 m-diameter primary mirror and a focal plane array containing 14 128x2000 pixels CCDs (McEwen et al., 2007). Also see http://hirise.lpl.arizona.edu/ for more information on the camera. Ten adjacent red (550-850 nm) CCDs produce typical images covering 6 x 12 km from a 300 km orbit, achieving resolutions of 0.25-0.32 m/px and S/N ratios of up to 200:1. Binning results in lower data volumes, but obviously decreases resolution. Aligned with the centre red CCDs are 2 CCDs each with blue-green (400-600 nm) and NIR (near infrared, 800-

1000 nm) filters, allowing color imaging over the central 1.2 km-wide image swath.

3. Theory

3.1 The shadow method

The main idea behind the method is that the brightness of shadows contains information on the optical depth of the overlying atmosphere. If the optical depth of the atmosphere and the aerosols therein becomes larger, then the brightness difference between a shadowed and a nearby sunlit comparison region becomes smaller. The translation of this difference into an optical depth is what we named "the shadow method".

For the version of the method used here we make several assumptions: (i) the surface is Lambertian; (ii) the atmosphere has the same scattering properties above shadowed and above sunlit comparison regions; (iii) all pixels in an analyzed pair of shadowed and sunlit comparison regions receive the same amount of diffuse radiation from the sky; (iv) the albedo of the surface is approximated with the measured TOA albedo (Top Of Atmosphere albedo); (v) the atmosphere has the same optical depth above all pixels of an analyzed pair of shadowed and sunlit comparison regions.

We define the observed orbiter image $I(i,j)$; the value of each pixel (i,j) gives intensity. We define $B(i,j)$ as the intensity of radiation reflected upward by the surface towards the camera. If there were no atmosphere, then $I(i,j)$ and $B(i,j)$ would be equal. However, having an atmosphere not all radiation contained in $B(i,j)$ will reach the camera because a certain fraction will obviously be scattered or absorbed during its way up. The size of this fraction depends on the optical depth of the atmosphere τ and on μ, which is the cosine of the emission angle.

Additionally, an important part of the observed photons did not have their last interaction with the surface of Mars but in its atmosphere, usually with an aerosol and in rare cases with a gas molecule. We presume that most aerosols are particles of airborne dust and have properties as published by e.g., Markiewicz et al. (1999) or Tomasko et al. (1999). Following this assumption, most of these photons have been reflected upwards by the surface, and scattered on a particle of airborne dust once during their way up. Some of the photons have been scattered twice or more times before reaching the camera, but during periods of average atmospheric optical depth these form a minor fraction. Another fraction has never touched the surface; coming from the sun these photons scatter on one or more particles and then go back into space. Whereas particles of airborne dust scatter backward only a tiny part of the photons that hit them, this fraction is in general very small. However, if the airborne dust is covered by ice, or if the common high altitude hazes of very small particles have a significant optical depth above the imaged region, then the fraction of these backscattered photons can become important. Together, all these photons that last scattered in the atmosphere invoke a diffuse glow above the surface of Mars. We name its contribution to the image $A(i, j)$. The atmospheric component $A(i, j)$ and the surface component $B(i, j)$ are not independent of each other. The aerosol scattering properties that we assume here and a scale height of optical depth of more than 10 km imply that $A(i, j)$ mainly is a spatial average of $B(i, j)$ over a region of order 100 km^2, multiplied with the atmospheric scattering fraction of $(1 - e^{-\tau/\mu})$ and, in colors between yellow and red, multiplied with 0.9–0.95 because 5–10% of the scattered photons are absorbed by the aerosols. We elaborate on this in Section 3.2.

The intensity $I(i, j)$ that is imaged by the orbiter scanners above the atmosphere will then be:

$$I(i, j) = B(i, j)e^{-\tau/\mu} + A(i, j)$$

or

$$I = Be^{-\tau/\mu} + A \qquad (1)$$

when omitting location subscripts i and j. Let F be the direct solar flux onto the surface, μ_0 the cosine of the solar incidence angle, and R_S the Lambert albedo of the surface. We define F_{diff} as the total diffuse flux onto the surface. Technically, it is the sum of diffuse flux from the sky and light that is reflected by the surrounding terrain, but the diffuse flux from the sky is by far the most important component. Let x_1 be the fraction of the diffuse radiation that reaches an analyzed spot on the surface in shadow and let x_2 be this fraction for a sunlit comparison region.

Thus we approximate:

$$B_{shad} = \frac{F_{diff}}{\pi} x_1 R_S$$

and (2)

$$B_{sunlit} = \frac{F}{\pi}\mu_0 R_S e^{-\tau/\mu_0} + \frac{F_{diff}}{\pi} x_2 R_S$$

Thus, the imaged intensity in the shadow I_{shad} is:

$$I_{shad} = B_{shad} e^{-\tau/\mu} + A_{shad} = \frac{F_{diff}}{\pi} x_1 R_S e^{-\tau/\mu} + A_{shad} \qquad (3)$$

and the imaged intensity in the sunlit comparison region I_{sunlit} is:

$$I_{sunlit} = (e^{-\tau/\mu_0} \frac{F}{\pi}\mu_0 R_S + \frac{F_{diff}}{\pi} x_2 R_S) e^{-\tau/\mu} + A_{sunlit} \qquad (4)$$

We take $A = A_{shad} = A_{sunlit}$; this follows from assumption (ii) made at the beginning of this section. This approximation should be quite accurate as long as a shaded region and its sunlit comparison region are less than a few kilometers apart and do not differ more than a few hundred meters in altitude because then these should almost always have a very similar atmosphere above them. I.e., considering that photons on average bounce of airborne dust under angles of around $\Theta = 20°$ (via the asymmetry parameter $\delta = \cos(\Theta)$ given by Markiewicz et al. 1999), and that most of this dust seems well mixed into the atmosphere (e.g., Hoekzema et al. 2010, Hoekzema et al. 2007, Thomas et al. 1999, and Jaquin et al. 1986) and thus resides at several kilometers altitude, the aerosol contribution probably is almost always nearly homogeneous over horizontal distances of less than a few kilometers.

The subtraction $I_{sunlit} - I_{shad}$ thus removes the aerosol component A so that:

$$\Delta I = I_{sunlit} - I_{shad} = (e^{-\tau/\mu_0} \frac{F}{\pi} \mu_0 R_S + \frac{F_{diff}}{\pi}(x_2 - x_1) R_S) e^{-\tau/\mu} \qquad (5)$$

By taking $x_1 = x_2$ the diffuse scattering term that contains F_{diff} disappears from (5) and the equation becomes easily solvable. Thus we get:

$$\Delta I = I_{sunlit} - I_{shad} = e^{-\tau/\mu_0} \frac{F}{\pi} \mu_0 R_S e^{-\tau/\mu} \qquad (6)$$

However, taking $x_1 = x_2$ is a grave simplification that introduces a substantial error. From this point we therefore distinguish between the real optical depth τ and our shadow method estimate of the optical depth τ_{shad}. These are related, but obviously not equal. We will investigate their relation (section 5.1) and try to find an empirical correction factor (sections 5.2 and 5.3) so that we can estimate τ once we know τ_{shad}.

Rewriting formula (6) yields:

$$\tau_{shad} = -\frac{\mu_0 \mu}{\mu_0 + \mu} \ln\left(\frac{\Delta I}{\mu_0 \frac{F}{\pi} R_S}\right) \qquad (7)$$

3.2 Approximation of the surface albedo

To solve equation (7) the surface albedo R_S is needed, but this usually is unknown. We therefore approximate the Lambert albedo of the surface with the measured TOA albedo:

$$R_S = \frac{\pi I_{sunlit}}{\mu_0 F} \qquad (8)$$

It is clear that this approximation cannot be generally correct because it neglects the atmospheric influence, and it introduces another substantial error. For orbiter observations of Earth this would be a bad approximation because in Earth's atmosphere there is much Rayleigh scattering on gas molecules and backscattering on thin cloud covers, yielding an important radiation field that is independent of the underlying surface. However, in colors between yellow and red the approximation probably is on average reasonable for scattering on common martian airborne dust. In this range, the dust diminishes contrast but does not introduce large differences between the average surface albedo and the average TOA albedo. Airborne dust particles show very strong forward scattering. In a single scattering event well over 90% of the red photons are scattered forward under angles of less than 45° (18°-23° on average), the remaining fraction is mostly absorbed, and only a small part of it is scattered to the side or backwards. Hence, as observed from an orbiting spacecraft, $A(i, j)$ is in the first place a diffuse and transparent picture of the surface itself. Its contribution to the observed image does not brighten or darken it very much between yellow and red because there is not much absorption in this wavelength range.

For shorter wavelengths however, there is more absorption, up to 20-25% per scattering event in blue (Pollack et al. 1995). Moreover, on Mars there often are thin whitish high altitude clouds (see e.g., Montmessin et al. 2007). These are difficult to find in downward looking images but are usually well visible in the limb. These thin clouds probably have not much influence on the TOA albedo in red, but may on the other hand significantly increase the TOA albedo towards the blue because Mars is so dark in blue. Together these effects imply that towards the blue the atmospheric contribution $A(i, j)$ becomes less determined by radiation that is reflected upward from the surface and more determined by radiation that is decoupled from the surface. Using the TOA albedo as an approximation of the surface albedo will obviously introduce errors in the shadow method anyhow, but these errors may thus be considerably larger in blue and green than in yellow and red.

Considering the above, we suspect that the shadow method in the here presented form is not well adapted for images taken in blue and green. For these colors the TOA and surface albedo will probably often differ significantly, and moreover, the difference may well depend on optical depth. This in turn implies that any empirical correction factor between the retrieved value τ_{shad} and the real value τ may vary significantly with optical depth. Our analyses presented in section 5.1 strengthen our suspicion. There we retrieve probably nearly correct pressure scale-heights from panchromatic images, which suggests that for their color the correction factor C is close to constant, but we do not find similar indications for the blue and green images.

3.3 Expected errors

The calibration of HRSC images is an ongoing process and over the years HRSC images have been distributed in several different versions. The shadow method is sensitive to offset errors; an offset error of 1% in the measured intensity to first order roughly yields an error in the estimated optical depth of 1% as well (via equation 7). The empirical correction factor C will largely compensate for such errors, but each calibration version of HRSC (or any other camera) will yield a slightly different C. In Section 5.2 we focus on results for calibration version 13, the most recent one at the moment of writing, but we also checked version 10 and this older version of the same images yields a correction factor C that is some 3% larger.

In Section 3.2 we argued that if the shadowed and the sunlit regions have an albedo that is close to the local average, then there will generally not be a large difference between the surface and the TOA albedo for images taken in colors between yellow and red. This implies that approximation (8) should be reasonably good, but obviously it is less than perfect and the approximation will yield errors in the retrieved τ_{shad}. For example: if the estimate of the albedo is wrong by 10%, then according to formula 7 this may result in an error in the estimate of τ_{shad} by almost 0.1.

Obviously, it is best to choose flat surface for the sunlit comparison regions, because the used value of μ_0, which has a big impact on the values of I_{sunlit} and R_S, is valid for flat surface and most slopes are either brighter or darker. If $\pi I/\mu_0 F$ is measured on inclined surfaces then it will usually over- or underestimate R_S when μ_0 is not corrected for the slope angle, and an imprecise approximation for R_S will as discussed yield an imprecise estimate of the optical depth τ_{shad}. In section 5.3.3 we use HiRISE images to show examples of effects caused by choosing regions with a wrong albedo or on a slope. Petrova et al. (submitted to Planetary and Space Science) shows examples in which they correct μ_0 for slope angles.

Differences between x_1 and x_2 will also introduce errors. Often x_2 will be somewhat larger than x_1 since the sunlit region will usually see (a bit) more of the sky than the shadowed region; such a difference decreases τ_{shad}. For example, for the observing geometry of the HiRISE image analyzed here (Section 4.3), and for $\tau_{shad} \approx 0.3$ and presuming that the shadowed region is next to a slope, but that this slope is far away and therefore not visible from the sunlit comparison region, this may result in $x_2 - x_1 \approx 0.1$. This would yield an error of about 0.06 (20%) in the retrieved τ_{shad}. This implies that the distance between the selected pixels in shadow and their sunlit comparison regions is important because it obviously largely determines the differences between x_1 and x_2. In Section 5.1 we present results from images for which we had not much choice except choosing sunlit comparison regions at wildly varying distances from the shadows to which these are paired, and this probably explains why the spread in the retrieved τ_{shad} is rather large. In Section 5.2 we varied the distance to illustrate and quantify the effects (the τ_{shad} retrieved from sunlit comparison regions that are far away from their shadows are 20-25% smaller than the τ_{shad} that were retrieved from close-by ones). In Section 5.3, we present retrievals for which x_1 is somewhat smaller than x_2, but the differences do not vary much so that it does not invoke a large spread.

The rims of fresh small craters that cast shadows will at the same time obscure part of the sky, and in particular the bright part below the sun just above the horizon. For such craters both x_1 and x_2 are smaller than for surrounding flat terrain, and inside the crater it will be smallest close to the parts of the rim that cast the shadows because here the wall appears largest and obscures the largest fraction of the sky. On average, sunlit regions in small steep craters will be darker than sunlit regions of similar albedo on surrounding terrain. Our approximation $R_S = \pi I / \mu_0 F$ will thus generally lead to underestimating it, which increases τ_{shad}. E.g., say the diffuse flux from the full sky is 30% of the total flux onto the surface and that in a sunlit comparison region x_2 is as low as 0.67 so that the sunlit comparison region receives only two thirds of this 30%. As a result, the estimated albedo (which is calculated from the intensity in the sunlit comparison region) will be about 10% too low and the estimated τ_{shad} will thus be increased by about 0.06.

Non-Lambertian effects will also contribute to the errors, and in section 5.1.3 we will argue that these are marginally significant; that is, at least for the data-sets analyzed here.

Considering the above, we expect differences of tens of percents between the retrieved τ_{shad} and the real optical depth τ. In sections 5.2 and 5.3 we will present results that show that the retrieved τ_{shad} is systematically smaller than τ. We presume that approximating $x_1 = x_2$ introduces the largest error.

3.4 Retrieving τ_{shad} with the shadow method

We used a pair of lines on the surface for each retrieval; one line of pixels inside a shadow and one that was sunlit for comparison. Using formulas (7) and (8), the difference between the average intensity of the line in shadow and that of the sunlit one yield an estimate of τ_{shad}, and the spread around these averages is used to estimate the 1σ error. Note that the 1σ error tells about the spread of the measurements, but very little about the probably largely systematic errors that are introduced by the several rough approximations. We choose our analyzed pixels on lines because that was easy to program and in section 5.3.2 we show that this does not hinder the achieved precision if the lines are longer than a short minimum length.

To minimize effects from albedo variations and from shading we tried to choose sunlit comparison regions on flat terrain and with the same albedo as the selected shadows (as far as we could judge this from the images). In Section 5.3.3 we experiment with sunlit comparison regions that vary in albedo, or are on slopes, to illustrate the sensitivity of the shadow method on choosing these regions badly.

Approximate location of Figure 1

4. Data

4.1 The HRSC images of Valles Marineris

For our search for relations between scale-height of optical depth and altitude, we used all nine HRSC images that were acquired during orbit 1944 of MEX on July 21, 2005. The area that was used for our analysis is shown in Figure 1, which shows part of the nadir image. It covers a region of almost 100 km wide in the east-west direction and 515 km long in the north-south direction and is located around the equator and 94° longitude. The solar longitude was 253.3° (late northern hemisphere autumn), and the true solar local time between 16.30 h and 17.00 h.

As discussed in Sect. 2 the nine HRSC channels observe the martian surface from various angles. As a result, there are differences between all nine observed images that are caused by the perspective. I.e., topography on the surface changes its appearance with changing viewing angles. These perspective differences can largely be taken out by reprojecting the images onto the corresponding DTM. For this study we use the products of such reprojections, these are so called ‘ortho-images’. Ideally, there would be no perspective differences between the ortho-images of a given region, but because images and DTMs have a limited spatial resolution we cannot expect perfect co-registration; for the images of this set the errors are a few tens of meters. Details on the software and photogrammetric processing techniques that were used to derive DTMs and ortho-images, are given by Scholten et al. (2005) and Gwinner et al. (2005).

The original data have a spatial resolution of a few tens of meters per pixel, for this study we used ortho-versions of the images at a spatial resolution that was reduced to 125 meter per pixel. The pixels of the ortho-images are float averages over tens of observed byte pixels, and their intensities are given with a precision of up to a factor of about eight or nine better than the original pixels. Thus, their intensity distribution is very much smoother than that of the original data.

For each pixel of each image, values for solar incidence, emission, and phase angles are available. At any given location there is less than 2° of difference in solar incidence angles between all nine images; over the images these vary from 66°-72°. For the nadir image, the emission angles range between 0° and 9°. For S2 and S1 the ranges are 22°-24° and 21°-23°, respectively, for P1 and P2 14°-17°, for blue and green 3.5°-9.5°, and for red and IR 17°-20°. The ranges for the phase angles are: S2 58°-72°, red 59°-72°, P2 60°-72°, blue 63°-77°, nadir 63°-78°, green 65°-80°, P1 68°-84°, IR 71°-87°, S1 73°-88°.

The surface elevation varies between almost 300 m below zero on the floor of Valles Marineris and 9050 m above zero for the highest mountains inside the Valles. The plains to the South of the canyon are at altitudes of about 6300-7300 m

Approximate location of Table 1

4.2 The HRSC images of Gusev

Table 1 offers information on the five analyzed HRSC stereo images that were taken of Gusev (175.4 E 14.6 S) during orbit 4165 of MEX. All five images are panchromatic.

Figure 1 shows the image taken by the nadir sensor. Various table mountains and the rim of the crater cast shadows that were large enough to be analyzed.

As for our study of Valles Marineris (Section 4.1) we used ortho-images at a spatial resolution that was reduced from a few tens of meters per pixel to 125 meter per pixel. Again, the intensities that are given for these 125 m pixels are eight or nine times more precise than those of the observed pixels.

Approximate location of Table 2

4.3 The HiRISE images of Victoria crater

Table 2 offers information on the three analyzed HiRISE images. The images, taken in blue-green, red, and NIR, show Victoria crater in Meridiani Planum (1.95 S, 5.53 W) at a time that Opportunity stood at the edge of the crater. Figure 7 shows the crater as imaged in red. The spatial resolution is 0.27 m/px (with 1 x 1 binning) in the red image and 0.54 m/px (with 2 x 2 binning) in the blue-green and NIR images.

The northern part of the crater is on average darker than the southern part for several reasons. Firstly, the crater is bowl shaped. The northern parts are tilted away from the sun, while the southern parts are tilted towards it. Moreover, due to the illumination angle, the northern rim casts much larger shadows than the southern one.

4.4 Optical depth measurements by the rovers Spirit and Opportunity

Around the time that the HRSC and HiRISE images analyzed here were taken, Spirit and Opportunity routinely measured the optical depth of the martian atmosphere, often a few times each day. They did so by looking into the sun through two special solar filters.

A red filter centered at 880 nm, and a blue filter which was intended to be centered at 440 ± 20 nm, but due to a red leak it was in effect centered at 719 nm. See Lemmon et al. (2004) for a discussion on MER's optical depth measurements and the suspected red leakage in the blue solar filter. Analyses of IMP (Imager for Mars Pathfinder) data show that the differences in the optical depth in the range 440-880 nm are probably less than 5% (Markiewicz et al. 1999). We do not know which of the two filters yields the measurements that are best for comparing with the various images that we study here, and therefore use their average. We assume here that, taking the given errors into account, the values that are measured by the rovers can be used as the true optical depth τ.

According to the 2011 version of the available opacity data, Opportunity measured 0.43 ± 0.03 in blue and 0.45 ± 0.04 in red almost two hours before the HiRISE images of Victoria crater in Meridiani were taken. The 2010 version of the data also mentions these values, but also offers measurements between 1-1.5 hours after the HiRISE image was taken: 0.52 ± 0.02, 0.52 ± 0.02, and 0.51 ± 0.02 in blue; and 0.53 ± 0.03 and 0.53 ± 0.02 in red. To us, it appears likely that the atmospheric opacity changed significantly in the roughly three hours between the measurements before and after the HiRISE observation. We do not know what the opacity was at the moment that HiRISE took the images; maybe it was still close to the earlier measurements, maybe it had already increased to around the later values, but probably it was somewhere in between. Therefore we take τ_{op}= 0.48 ± 0.05, assuming that the large error range includes the real value.

According to the 2011 version of the data, Spirit measured values 0.73 ± 0.04 and 0.75 ± 0.02 in blue, and 0.76 ± 0.04 and 0.78 ± 0.02 in red, around the time that the HRSC images were taken. The differences with the 2010 version of the data are not large. We take τ_{sp}= 0.76 ± 0.03 in Gusev.

5. Results and discussion

5.1 The scale-height of optical depth in Valles Marineris from HRSC images

5.1.1 General

We present results from a shadow method analysis of nine HRSC images. These nine images together form a set of stereo and color images of an area in and around Valles Marineris. The area covers an altitude range of about 8 km so that we can investigate how the shadow method retrievals depend on altitude. Figure 1 shows examples of selected regions in shadow (indicated in white) and sunlit comparison regions (indicated in black) overlaid onto the nadir image. Each region in shadow is paired to a nearby sunlit one; each pair yields a retrieval of τ_{shad}.

Results presented in Section 5.2 indicate that selecting sunlit comparison regions that are close to the analyzed shadows minimizes the spread in the retrievals, and thus increases the precision of the retrieved τ_{shad}. However, for the here analyzed images it proved undoable to find sunlit comparison regions that were close to usable shadows, and on flat surface, and that also sample the surface altitudes sufficiently. We therefore allowed sunlit comparison regions to have considerable distances from their shadows, and instead selected a large amount of pairs, more than 150 in each image, trying to reduce errors by averaging over a lot of retrievals.

All pairs were manually selected from the P1 image (an arbitrary choice) and for images of the eight other channels we used the same pixel locations. A given pixel-location corresponds to the same locations on Mars within a few tens of meters in all nine images. If the location of a pixel showed an imaging error in any of the nine used images, then the location was excluded from our analysis. This happened to 1-2% of the pixels.

The altitude that we assign to an analyzed region is the average altitude of the sunlit comparison region, not that of the shadowed one, because generally the DTM (Digital Terrain Model) is more reliable in a sunlit region. We selected each sunlit comparison region so that it differed less than a few hundred meters in altitude with the shadowed region to which it was paired. The difference typically is 100-200 m.

Approximate location of Figure 2

5.1.2 The scale-height of optical depth from the panchromatic images

Figure 2 shows the results for the five panchromatic stereo images. The τ_{shad} that are derived from these are plotted versus altitude. The smooth curves in the plots are Linear Mean Square Regression fits on the natural logarithm of the τ_{shad} versus altitude.

The individual measurements are plotted with one sigma error ranges as measured from the spread (see section 3.4). The error ranges that are given for the individual measurements seem quite reasonable. Possibly these overestimate the measurement uncertainty a bit, because only about a sixth of the measurements are outside the one sigma range, whereas this would be a third in the ideal case. We note that the given one sigma error ranges offer an estimate for random measurement errors and not for systematic differences between τ_{shad} and the true optical depth τ .

The five panchromatic images yield five estimates of the scale-height of optical depth in the Valles. Their average is 12.2 ± 0.7 km. This range covers the value of 12-13 km that is predicted by the http://www-mars.lmd.jussieu.fr/ climate database. Our retrievals agree with a well mixed atmosphere with an average temperature in this region of

236 ± 14 K, which is similar to expected range for this equatorial range before sunset according to the above mentioned climate database which suggests 232-240 K during periods with average dust loading.

In Sections 5.2 and 5.3 we offer results of analyses of panchromatic HRSC images and of a red HiRISE image. These analyses suggest that τ_{shad} is roughly two thirds of τ. Thus, τ_{shad} and the true optical depth τ are not equal. However, the main conclusion of this sub-section is that for the analyzed panchromatic images C (the correction factor between τ_{shad} and τ) appears to be almost independent of optical depth (altitude). Otherwise the retrieved values of τ_{shad} would simply not yield the expected scale-height. (That is: if the pressure scale-height is indeed similar to the scale-height of optical depth and if it is indeed about 12-13 km as expected from the consulted GCM.)

5.1.3 On phase angles and the Lambertian approximation

One may not expect that the martian surface is Lambertian. Other regolith surfaces such as the surface of the Moon (e.g., Kreslavsky et al., 2000) or Mercury (e.g., Ksanfomality et al. 2007) certainly are not. However, the shadow method, in the form in which it is used here, assumes the simplest case and does use a Lambertian approximation. The differences between the results for the five panchromatic images, which obviously differ in phase angle, offer some indication on the loss of accuracy resulting from using this approximation. For any given location the phase angle differences between the images are less than 15°-16° (see Section 4.1). However, differences between the results for the five panchromatic images are not only caused by non-Lambertian behavior, but also by the spread displayed by any set of measurements of limited precision. It is not clear how these effects can be fully separated, but of course the observed spread in our results does indicate an upper limit for the effects introduced by using the Lambertian approximation.

The lower right hand panel of Figure 2 shows the five fits of optical depth versus altitude together in one plot. The differences between the five fits are smallest near the bottom of the Valles; here the range is 0.53-0.55. The range is larger at high altitudes (range 0.26-0.30). Towards higher optical depths the five fitted curves approach each other and the one sigma spread between them is less than 5% when τ_{shad} is around 0.5. Towards lower optical depth the spread grows to about 10% for $\tau_{shad} \approx 0.3$. Thus, at least for the range in our sample, the shadow method appears to become more precise if the amount of airborne dust increases.

Probably the differences in phase angle have a marginally significant effect on the correction factors between true optical depth τ and shadow method measurement τ_{shad}. P2 and S2 yield slightly lower scale-heights than P1 and S1; the difference is around 0.7 km which is marginally larger than the 1σ error range of 0.5-0.6 km that is assigned to each fit. The nadir image, which as far as we understand, should yield an intermediate value because it has intermediate phase-angles, but actually yields a scale-height that is roughly 1.2 km smaller. This is approximately a 2σ effect. Over the years we have analyzed several hundreds of HRSC images and noticed that nadir images tend to be a few percent darker than the other panchromatic ones, there may be a connection to this 2σ effect. On the other hand, it may also be an unexpected effect from e.g., scattering on aerosols.

The main conclusion from this sub-section is that phase angle related differences are significant, but not strongly significant, for the analysis of these images of Valles Marineris.

Approximate location of Figure 3

5.1.4 The scale-height of optical depth from five different HRSC color images

Figure 3 shows optical depth as a function of altitude in the Valles Marineris as derived from the blue, green, red, and NIR color images, as well as the nadir one. The spread between the optical depth retrievals τ_{shad} is similar to that of the panchromatic channels displayed in Figure 2. All results from the red image are very similar to that of the panchromatic ones.

From blue towards red the fits show a smooth trend of decreasing τ_{shad} and the scale heights that are derived from these also decrease, NIR shows a slightly different curve (see discussion below). Around 8 km altitude the measured τ_{shad} in blue is about 0.37, and in red and nadir τ_{shad} is about 0.27—0.29: thus these differ by a factor of around 1.32. Close to 0 km altitude τ_{shad} is near 0.58 for blue and 0.54 for red and nadir; here the factor is around 1.07. This trend is also visible in figure 4, which shows the average measured τ_{shad} for five different altitude intervals. Near the bottom of Valles Marineris τ_{shad} does not vary by more than $\Delta\tau_{shad} \approx 0.05$ between blue and NIR, but at higher altitudes it is clearly largest in blue.

Approximate location of Figure 4

The derived scale-heights of optical depth change with wavelength, which is visible in figure 5, where these scale-heights are shown as a function of wavelength. For blue and green these are 17.0 ± 0.7 km and 14.5 ± 0.5 km respectively, and both values are larger than the expected pressure scale-height of 12-13 km (via http://www-mars.lmd.jussieu.fr/). Thus whereas the panchromatic and red images yield values (12.2 ± 0.7 km and 12.5 ± 0.5 km respectively) that are very similar to the expected pressure scale-height, the blue and green ones do not. Thus, it is possible that the correction factor varies significantly with optical depth for blue and green images; in any case these results do not offer prove that it does not.

In Section 3.2 we predicted that the shadow method would work better for red and yellow images than for blue or green images because the atmospheric contribution is more strongly coupled to the surface in yellow and red; we indeed see this in the results presented here. Possibly the thin whitish hazes that are common in the atmosphere of Mars at altitudes above some 50 km (see e.g., Montmessin et al. 2007) are especially important in this respect. These clouds are not homogeneously mixed with the air and if there is a distinct cloud layer that covers the full region at higher altitudes, then estimating the scale-height of the airborne dust below the layer results in an overestimation. A result of Hoekzema et al. (2010) may be instructive in this context. They analyzed a region inside the Valles Marineris where stereo method measurements yield a very high estimate of the scale height of optical depth, probably because of dust clouds above the Valles. Thin white high altitude hazes may similarly lead to an estimate of the scale-height that is too high. However, it may well depend on color how much the scale-height is overestimated. Mars is bright between yellow and NIR, and for these colors the relative contribution of these hazes to the total measured intensities is small, meaning that these have little influence on the retrieved scale-heights. In blue, the martian surface can be five times darker. As a consequence, the relative contribution of such thin whitish high altitude hazes can become increasingly important towards the blue, meaning that their influence on the retrieved scale heights may become important.

Approximate location of Figure 5

We now turn to the results for the NIR image. At altitudes of around 8 km the optical depths that are derived from the NIR image are similar to those that are derived from the panchromatic and red images, but near 0 km these are about 8% larger. As a result, the scale height H of optical depth that is derived from the NIR image is smaller than the ones that are derived from the panchromatic and red images (H = 10.6 ± 0.4 km versus H = 12.2 ± 0.7 km). We may explain this in terms of a sounding of different size distributions.

Most martian dust particles presumably have sizes of 1-2 μm (see e.g., Markiewicz et al. 1999). However, the dust particle size distribution depends on altitude. The heavier large particles remain at lower altitudes whereas lighter small particles are well-mixed up to higher altitudes (see Wolff et al., 2006). Thus, in the lower atmosphere the particles are on average larger than higher up.

With increasing photon-wavelength the effective scattering cross section of an aerosol decreases when this wavelength becomes larger than roughly the size of the aerosol. If the aerosol effective radius is indeed smaller at higher altitudes than at lower altitudes, then photons with NIR wavelengths are scattered more readily on the average aerosol in the lower atmosphere than on the average aerosol higher up, leading to an increase in optical depth that is stronger than the increase in gas-pressure when descending through the atmosphere. In summary, our results are consistent with a picture in which the dust particle size increases towards the bottom of Valles Marineris.

Our main conclusion from this sub-section is that it is safest to use images that are taken in colors between yellow and red for the shadow method.

Approximate location of Figure 6

5.2 Near Spirit: τ_{shad} derived from panchromatic HRSC images

Spirit measured an optical depth $\tau_{sp} = 0.76 \pm 0.03$ around the time that HRSC took the S1, P1, nd, P2, and S2 images analyzed here (see Table 1). The images show shadows inside the rim of Gusev crater in a region around 100 km to the south of the Spirit rover. The range of measured TOA albedos in these regions is 0.25-0.29 and the shadows in the images on average have a brightness of between 75-80% of the surrounding flat sunlit terrain. The upper panel of Figure 6 shows the shadowed regions (white lines) and sunlit comparison regions (black lines) of, what we assume is, our best selection. We selected these sunlit comparison regions close to the shadows to minimize the differences in diffuse illumination and used the DTM to choose reasonable flat terrain to minimize the influence from shading induced by the surface topography. A minor complication is that three of the analyzed regions are significantly above the altitude of the Spirit rover. Therefore, we also give, together with the retrieved value of τ_{shad}, values that are corrected for this altitude difference by increasing it according to a 12-14 km scale-height of optical depth. Table 3 offers the results.

Corrected for their altitudes, the retrieved τ_{shad} range between 0.50 and 0.60 while their average is $\tau_{shad} = 0.54 \pm 0.02$. The spread between the retrievals is much smaller than their differences with Spirit's measurement τ_{sp}. If we follow up on our conclusion from Section 5.1 that in the color of the panchromatic channels there is a more or less constant correction factor C between τ_{shad} and the real optical depth $\tau\ (\approx \tau_{sp})$, and that this factor is almost independent of the optical depth, then it has the value $C = \tau_{shad} / \tau \ = 0.71$. Before assigning an error to this value, we discuss the importance of where one chooses the sunlit comparison regions.

In section 3.3 we argued that the value of the correction factor is quite sensitive to the difference between the diffuse illumination of a shadowed region and of its sunlit comparison region. The diffuse illumination onto a location depends on how much of the sky is blocked from view by the surrounding topography and thus the correction factor depends on the surrounding topography as well. In the analysis of Gusev crater as presented in the upper panel of Figure 6 we took care to select sunlit comparison regions that are close to the analyzed shadows. This yielded a correction factor of C = 0.71, and this was an upper limit. I.e., sunlit comparison regions at larger distances always yielded smaller values.

The lower panel of Figure 6 shows an example of choosing the sunlit comparison regions at such large distances that the slopes that cast the shadows are hardly or not visible from the sunlit comparison regions. The average of the retrieved τ_{shad} is 0.39 ± 0.01 for the nadir image and 0.01-0.02 higher in the other four images. When also correcting for the altitude differences with the rover we find $\tau_{shad} = 0.41 \pm 0.01$. This corresponds to a correction factor C = 0.54, and in our sampling this was the lower limit.

Moving the sunlit comparison regions towards the mountains that cast the shadows increased the retrieved τ_{shad} and the corresponding correction factors gradually, until the correction factor reached the upper limit of C = 0.71 when the regions are just outside the shadows. Thus, we did not find correction factors outside the range C = 0.63 ± 0.09, and this suggests that, at least for this dataset, dividing τ_{shad} by C = 0.63 ± 0.09 yields a good estimate of the real optical depth τ. The assigned error is almost ±15%, and arises solely from the range in measured correction factors. Technically, it should be combined with the errors from other sources, but in this case these are probably hardly significant. However, a better selection of the sunlit comparison regions will give a much smaller range of correction factors, and then these other errors probably are important. E.g., for the images of Gusev that we studied here, we could, and in the first place did, choose sunlit comparison regions close to the shadows and the resulting spread in the retrieved τ_{shad} is only ± 3%. We combine it with educated guesses and estimates of other errors.

Using the Lambertian approximation also introduces an error, possibly up to ± 5% (Section 5.1.3). We assigned an error of ± 4% to the optical depth measurement by Spirit (Section 4.4). Moreover, offset errors in the intensity calibration of HRSC may cause errors of around ± 4%. We arrive at this value by comparing different versions of the

HRSC data; all the results that were presented in this Section are for calibration-version 13, the most recent one at the moment of writing. Using older versions yields slightly different results. Where version 13 yielded a correction factor of C = 0.71, version 10 for example yielded C = 0.73. Combining these errors from four different sources yields an overall error of maybe ± 8% in the derived average correction factor.

Concluding, this analysis of Gusev images suggests that $\tau_{shad} = (0.63 \pm 0.09) * \tau$ if the sunlit comparison regions are at varying, more or less arbitrary, distances from the shadows, and $\tau_{shad} = (0.71 \pm 0.06) * \tau$ if the sunlit comparison regions are close to the shadows.

Obviously, these results are derived from a single set of HRSC images and this does not prove that other good orbiter images necessarily yield similar correction factors. Nowadays, there are several other sets of usable orbiter observations of Meridiani and Gusev and hopefully more observations will follow. We plan to use these for a more elaborate validation study in the future, but for this paper we limit ourselves to one other case-study that we describe in the next Section.

Approximate location of Table 3

5.3 Near Opportunity: τ_{shad} derived from HiRISE imagery

5.3.1 General

In Section 5.1 we showed that images taken in colors between yellow and red have a correction factor that shows little dependence on optical depth. In Section 5.2 we measured correction factors for a set of HRSC images. In this section we present results from an analysis of HiRISE images of the exploration site of the Opportunity rover at Victoria crater in Meridiani. This region is much darker than Gusev, and the images have a spatial resolution that is between 300 and 500 times higher than the HRSC images of Section 5.2. These very different data can give an indication of how much such correction factors depend on the camera used, on the spatial resolution of the analyzed images, and on the albedo. We investigate these points in sections 5.3.2 and 5.3.3.

While parked at the edge of the crater, Opportunity measured an optical depth τ_{op} = 0.48 ± 0.05 around the time that HiRISE took the images analyzed here. (Note that the uncertainty in this measurement by Opportunity is significantly larger than that in Spirit's one used in Section 5.2.) Figure 7 and 8 both show parts of the red image. The analyzed locations in shadow are indicated in white; these shadows were all cast by the northern rim of the crater. In the red and NIR images their brightness is 58-61% of that of the flat region near the center of the crater; in the Blue-Green one the range is 64-66%. Each retrieved τ_{shad} is printed next to the black line that indicates the sunlit comparison region that was used for the retrieval.

5.3.2 Flat sunlit comparison regions

In this subsection we try to minimize the influence from shading. Obviously, slopes can cause shading and therefore we here choose the sunlit comparison regions around the central region of Victoria crater because this is the flattest part of the bowl-shaped crater. The central region has a Top Of Atmosphere (TOA) albedo = $\pi I/\mu_0 F$ of around 0.14 in the red image analyzed here; we use this as the value of the albedo in our shadow method formula. (To explore the sensitivity of the retrievals on albedo, we will analyze sunlit comparison regions with higher and lower TOA albedos in the next sub-section.)

Twenty retrievals with our shadow method thus yielded on average $\tau_{shad} = 0.324 \pm 0.016$. The spread between these twenty retrievals is remarkably small; nineteen are within 0.02 of the average. Thus, as for the described retrievals from HRSC images in the previous section, the factor between τ_{shad} and τ_{op} (.τ) is almost fully systematic. As in Section 5.2, we assume that the Lambertian approximation introduces errors of at most ± 5%, and that the uncertainty in the calibration of the camera introduces at most ± 3%. The spread in the retrievals is ± 5%, and the accuracy in Opportunity's measurement is ± 10%. This yields a correction factor $C = \tau_{shad} / \tau = 0.68 \pm 0.09$. The error is mostly determined by the uncertainty in the optical depth that Opportunity measured on the surface.

We also analyzed the NIR and the blue-green images of Victoria crater and for that used the same twenty locations for shadowed and sunlit comparison regions. The NIR image yielded a result that is very similar to that for the red image: $\tau_{shad} = 0.309 \pm 0.014$ and a correction factor of $C = 0.64 \pm 0.09$. However, the blue-green image yielded clearly larger values: $\tau_{shad} = 0.378 \pm 0.016$ and a correction factor of $C = 0.79 \pm 0.10$; this is comparable with our results from Section 5.1.4 where τ_{shad} derived from blue images was also larger than τ_{shad} as derived from yellow to red images. We note that our results from Section 5.1 suggest that giving correction factors for NIR and especially for blue-green is of limited use because we have no proof that these are independent of optical depth.

We experimented with the location of the analyzed shadow pixels. For several of the twenty retrievals we selected pixels near the edge of shadows and for other ones and we choose the pixels closer to the centre; we used the largest shadow for ten retrievals and three smaller ones for the other ten. It appeared to be unimportant which shadow we choose, or which part of it; the impact on the retrieved τ_{shad} is not noticeable. Checking the spread of intensity $\pi I/\mu_0 F$ gave us an indication why; we calculated an average $\pi I/\mu_0 F$ over the twenty shadowed and an average over the twenty sunlit comparison regions and the spread around these. For the red image, the average of the shadowed regions is: 0.0840 ± 0.0016 and for the sunlit ones it is: 0.140 ± 0.004. Thus, the spread for the latter is 2-3 times larger than for the first. For blue-green and NIR we also found that the effects from the spread in intensity in the sunlit regions dominate over the spread from the shadowed ones.

The central area of the crater is almost flat, except for ripples that cover parts of it. Several of our twenty sunlit comparison regions cross ripples, and several do not (we choose the latter in the nearly flat but almost not rippled area just eastward). There is no significant difference in the results between these two categories. Thus, the rippling appears to be of minor importance for the retrievals.

We experimented with the size of the sunlit comparison regions. Decreasing their size increased the spread in the results; it seems obvious that this is a result of an increasing Poisson error. From the twenty regions of the sample discussed here, two are examples of this. One of these is the single retrieval from the red image that deviates by more than 0.02 from the average of the shadow method retrievals (0.28 versus 0.324).

In conclusion, using twenty sunlit comparison regions that are located in the flattest part of Victoria crater yielded optical-depth-retrievals τ_{shad} with a small spread of only ± 5%. However, the difference between τ_{shad} and τ is large, but whereas it is almost fully systematic in nature it can be compensated for by using a correction factor C. For the red image we found a factor $C = \tau_{shad}/\tau \; = 0.68 \pm 0.09$

The correction factors measured from the panchromatic HRSC images and the HiRISE red image are comparable. In particular, the studied panchromatic HRSC images of orbit 4165 commonly yield very similar correction factors when choosing the sunlit comparison regions at some distance, but not too far away, from the slope that casts the shadow (see Section 5.2). Obviously, this is also the case for the HiRISE image. Thus, although the spatial resolution of the HRSC images is between 300 and 500 times less than that of the HiRISE ones, and although the observations are taken by different cameras, and although Gusev is a bright red dust region while Meridiani is exceptionally dark, we still find rather similar correction factors.

Approximate location of Figure 7

5.3.3 The impact of slopes and albedo variations in and around Victoria crater.

The results of the shadow method depend strongly on albedo and slope of the sunlit comparison regions. We offer examples to illustrate this. These effects from albedo and slope appeared very similar for the blue-green, the red, and the NIR images and therefore we only offer results and discussion for the red one.

In Figure 7, the regions indicated by letters show results for retrievals that use sunlit comparison regions in the southern part of the crater. This part is tilted towards the sun and, as explained in Section 3, because of this we expect the shadow method to underestimate the optical depth here. I.e., we approximate the surface albedo R_S with $\pi I/\mu_0 F$, but on this slope this is inaccurate because we use a value for the cosine of the solar incidence angle, μ_0, that is correct for flat terrain. Meaning, since we ignore the brightening from the slope being tilted a bit towards the Sun we derive an albedo that is higher than it would be for the flat terrain. The retrieved τ_{shad} are in the range 0.28—0.30, which is indeed lower than those for the flatter terrain around the center of the crater, but only by about 11%.

Figure 8 shows the northern rim of Victoria carter and results for a line of shadow pixels that is compared with various sunlit regions. First we compare these shadow pixels with two nearby sunlit regions (G and H); this close proximity presumably makes differences in diffuse illumination unimportant. Nevertheless the results, $\tau_{shad} = 0.65 \pm 0.07$ and $\tau_{shad} = 0.63 \pm 0.06$ are about two times higher then the retrievals from the flattest terrain because the regions are on a steep scree slope that, because it is tilted away from the sun, is quite dark so that we underestimate the albedo. Petrova et al. (submitted to Planetary and Space Science) use the DTM of Victoria crater to correct for such effects.

Next, we selected two sunlit regions slightly downward (I and J) on a less steep part of the same slope; this yielded $\tau_{shad} = 0.47 \pm 0.03$ and $\tau_{shad} = 0.46 \pm 0.02$, which happens to be close to the ground-truth, but presumably this agreement is accidental. This illustrates that it is best to avoid choosing sunlit comparison regions on slopes, especially if these are tilted away from the sun.

Our shadow method approximation is based on the assumption that the shadowed and the sunlit regions have the same albedo. We now explore the impact of deliberately choosing sunlit comparison regions on flat terrain, just outside the crater, that have a somewhat wrong albedo. Areas C and D display a brightness of $\pi I/\mu_0 F \approx 0.14$, which is about average for this regions, and yield values of $\tau_{shad} = 0.33 \pm 0.03$ and 0.32 ± 0.02 respectively. Dividing these by the correction factor yields values close to Opportunity's value of $\tau_{op} = 0.48 \pm 0.05$. The brightest regions that we analyzed (E and F) had $\pi I/\mu_0 F \approx 0.16$ and yielded τ_{shad} = 0.27 ± 0.03. Starting at the rim of Victoria crater, a few dark streaks extend northwards. We selected two comparison regions inside a dark streak (A and B), with $\pi I/\mu_0 F \approx 0.115$ and $\pi I/\mu_0 F \approx 0.118$ these yielded τ_{shad} = 0.45 ± 0.02 and τ_{shad} = 0.46 ± 0.02 respectively, which is close to the Opportunity's value, but obviously is much too high if we apply the correction factor.

Our main conclusion from this subsection is that it is clearly important to choose flat sunlit comparison regions and to especially avoid selecting them on terrain with a much lower albedo than the shadowed regions or on slopes that are turned away from the sun.

Approximate location of Figure 8

ACCEPTED MANUSCRIPT

6. Conclusions

We found indications that our simplified version of the shadow method can be used to estimate the optical depth of the martian atmosphere with an accuracy of better than ± 15%. That is, from images taken in colors between roughly 600-800 nm, and by selecting pairs of shadowed and flat sunlit comparison regions that have about the local average albedo.

We came to this conclusion in two steps. In Section 5.1 we argue that shadow method retrievals from images taken in yellow to red colors very likely yield a quite accurate estimate of the local scale height of optical depth; that is: in the likely case that the scale height of optical depth is similar to the pressure scale-height. This is a strong indication that such retrievals are close to proportional to the true optical depth.

In Sections 5.2 and 5.3 we analyzed HRSC and HiRISE images respectively and these indicate that dividing the result of a shadow method analysis by an empirical correction factor $C = 0.63 \pm 0.09$ yields a good estimate of the true optical depth. If the sunlit comparison regions are close to the shadows, then the retrievals are probably more accurate and the correction factor may be $C = 0.71 \pm 0.06$. However, these results are based on the analysis of only two datasets and more datasets should be analyzed to improve the statistics.

We formulated the mathematics behind the shadow method and introduced several rough approximations to make the equations more easily and rapidly solvable. The assumed approximation that regions in shadow and their sunlit comparison regions receive the same amount of diffuse radiation, which obviously is not true, probably largely explains why the shadow method retrievals are systematically smaller than the real optical depth. Another rough approximation is that the surface albedo is similar to the TOA albedo. This may be a bad approximation for images taken in blue and green, especially because the ratio of surface and TOA albedo may depend significantly on optical depth; this probably explains why the shadow method does not work very well for these images. On the other hand, the approximation is probably reasonable between yellow and red and the shadow method yielded good results for the here analyzed images taken in these colors.

Acknowledgements

We thank Mark Lemmon for his help in interpreting the optical depth measurements of Spirit and Opportunity and two anonymous referees for various valuable comments on the original manuscript.

We thank the HiRISE team as well as the HRSC Experiment Teams at DLR Berlin and Freie Universitaet Berlin and the Mars Express Project Teams at ESTEC and ESOC for their successful planning and acquisition of data as well as for making the processed data available.

We acknowledge the effort of the HRSC and of the HiRISE Co-Investigator Team members and their associates who have contributed to this investigation in the preparatory phase and in scientific discussions within the Teams.

References

Angelats i Coll, M., Forget, F., López-Valverde, M.A., González-Galindo, F.,2005. The first Mars thermospheric general circulation model: The martian atmosphere from the ground to 240 km. Geophysical Research Letters, Volume 32, Issue 4

Chassefière, E., Drossart, P., Korablev, O., 1995. Post-Phobos model for the altitude and size distribution of dust in the low martian atmosphere. Journal of Geophysical Research 100, pp 5525-5539

Grassi, D., Formisano, V., Forget, F., Fiorenza, C., Ignatiev, N. I., Maturilli, A., Zasova, L.V., 2007. The martian atmosphere in the region of Hellas basin as observed by the Planetary Fourier Spectrometer (PFS-MEX). Planetary and Space Sciences 55, pp. 1346-1357

Gwinner, K., Scholten, F., Giese, B., Oberst, J., Jaumann, R., Spiegel, M., Schmidt, R., Neukum, G. und das HRSC Co-Investigator Team, 2005. Hochauflösende Digitale Geländemodelle auf der Grundlage von Mars Express HRSC-Daten. Photogrammetrie-Fernerkundung-Geoinformation 5/2005, p. 387-394.

Hoekzema, N.M., Garcia Comas, M., Gwinner, K., Grieger, B., Markiewicz, W.J., Keller, H.U., 2007. The Scale-Height of Dust around Pavonis Mons from HRSC Stereo Images, 2007LPICo1353.3154H Seventh International Conference on Mars, LPI Contribution No. 1353, p.3154.

Hoekzema, N.M., Garcia Comas, M., Stenzel, O.J., Markiewicz, W.J., Gwinner, K., Keller, H.U., 2010. Optical depth and its scale height in Valles Marineris from HRSC stereo images Earth and Planetary Science Letters, Volume 294, Issue 3-4, p. 534-540.

Inada, A., Garcia Comas, M., Atieri, F., Gwinner, K., Poulet, F., Bellucci, G., Keller, H.U., Markiewicz, W.J., Richardson, M.I., Hoekzema, N.M., Neukum, G., Bibring, J.-P., 2008. Dust haze in Valles Marineris observed by HRSC and Omega onboard Mars Express. Journal of Geophysical Research 113, CiteID E02004

Jaquin, F., Gierasch, P., Kahn, R., 1986. The vertical structure of limb hazes in the martian atmosphere, Icarus 68, 442-461.

Jaumann R., Neumum G., Behnke T., Duxbury T.C. Eichentopf K. Flohrer J., Van Gasselt S., Giese B., Gwinner K., Hauber E., Hoffmann H., Hoffmeister A., Koehler U., Matz K.D., McCoed T.B., Mertens V., Oberst J., Pischel R., Reiss D., Ress E., Roatch T., Saiger P., Scholten F., Schwarz G., Stephan K., Waelisch M., and the HRSC Co-Investigator Team, 2007. The high-resolution stereo camera (HRSC) experiment on Mars Express: Instrument aspects and experiment conduct from interplanetary cruise through the nominal mission, Planetary and Space Sciences 55, pp. 928-952

Johnson, J.R., Grundy, W.M., and Lemmon, M.T., 2003. Dust deposition at the Mars Pathfinder landing site: observations and modeling of visible/near-infrared spectra, Icarus 163, 330-346

Lemmon, M., Wolff, M.J., Smith, M.D., Clancy, R.T., Banfield, D., Landis, G.A., Ghosh, A., Smith, P.H., Spanovich, N., Whitney, B., Whelley, P., Greeley, R., Thompson, S., Bell, J.F., Squyres, S.W., 2004. Atmospheric Imaging Results from the Mars Exploration Rovers: Spirit and Opportunity, Science 306, 1753-1756

Kahn, R., Goody, R., and Pollack, J.B., 1981. The martian twilight, Journal of Geophysical Research 84, pp. 5833-5838.

Kreslavsky M.A., Shkuratov Yu.G., Velikodsky Yu.I., Kaydash V.G., Stankevich D.G., 2000. Photometric properties of the lunar surface derived from Clementine observations, Journal of Geophysical Research 105, E8, pp. 20281-20295

Ksanfomality L., Harmon J., Petrova E., Thomas N., Veselovsky I., Warell J., 2007. Earth-Based Visible and Near-IR Imaging of Mercury, Space Science Reviews, 132(2-4), 351-397, 2007; DOI: 10.1007/s11214-007-9290-3

Markiewicz, W.J., Petrova, E.V., Hoekzema, N.M., Inada, A., Keller, H.U., Gwinner, K., Hoffmann, H., Neukum, G., HRSC Co-Investigator Team / The retrieval of atmospheric optical depth and surface albedo of Mars from the brightness of surface shadows in the

HRSC images / European Geosciences Union, General Assembly 2005, Vienna, Austria, 24-29 April 2005

Markiewicz, W.J., Sablotny, R.M., Keller, H.U., Thomas, N., Titov, D., Smith, P.H., 1999. Optical properties of the martian aerosols as derived from Imager for Mars Pathfinder midday sky brightness data, Journal of Geophysical Research 104, Issue E4, 9009-9018.

McEwen, A.S., Eliason, E.M., Bergstrom, J.W., Bridges, N.T., Hansen, C.J., Delamere, W.A., Grant, J.A., Gulick, V.C., Herkenhoff, K.E., Keszthelyi, L., Kirk, R.L., Mellon, M.T., Squyres, S.W., Thomas, N., Weitz, C.M., 2007. Mars Reconnaissance Orbiter's High Resolution Imaging Science Experiment (HiRISE), Journal of Geophysical Research (Planets) 112, 5.

Montmessin, F., Gondet, B., Bibring, J.-P., Langevin, Y., Drossart, P., Forget, F., Fouchet, T., 2007. Hyperspectral imaging of convective CO_2 ice clouds in the equatorial mesosphere of Mars, Journal of Geophysical Research, 112, Issue E11, CiteID E11S90

Neukum, G., Jauman, R. and the HRSC Co-Investigator Team, 2004. HRSC: The High Resolution Stereo Camera of Mars Express. ESA Special Publications SP-1240.

Petrova, E., Hoekzema, N.M., Markiewicz, W.J., Thomas, N., Shadows in an HiRISE image: a modeling attempt to retrieve the optical thickness. Submitted to Planetary and Space Science.

Pollack, J.B., Ockert-Bell, M.E., Shepard, M.K., 1995. Viking Lander image analysis of martian atmospheric dust. Journal of Geophysical Research 100, Issue E3, 5235-5250

Scholten, F., Gwinner, G., Roatsch, T., Matz, K.-D., Wählisch, M., Giese, B., Oberst, J., Jaumann, R., Neukum, G. and the HRSC Co-Investigator Team, 2005. Mars Express HRSC Data Processing - Methods and Operational Aspects. Photogrammetric Engineering & Remote Sensing 71(10), pp. 1143-1152.

Stenzel, O.J., Hoekzema, N.M., Markiewicz, W.J., Keller, H.U., 2007, and the HRSC co-investigator team, 2007. A Simple Scheme for Batch Processing Atmospheric Correction of HRSC Colour Images. European Mars Science and Exploration Conference: Mars Express & Exo Mars, Noordwijk, Netherlands, November 12-16, 2007

Stenzel, O.J., Hoekzema, N.M., Markiewicz, W.J., Keller, H.U., 2008. Correction of HRSC Images for Atmospheric Dust Using a Simple Optical Depth Retrieval Method. Conference on “Mars Atmosphere: Modeling and Observations”, Williamsburg, USA, November 10-13, 2008.

Thomas, N., Britt, D.T., Herkenhoff, K.E., Murchie, S.L., Semenov, B., Keller, H.U., Smith, P.H., 1999. Observations of Phobos, Deimos, and bright stars with the Imager for Mars Pathfinder, Journal of Geophysical Research 104, Issue E4, 9055-9068

Tomasko, M.G., Doose, L.R., Lemmon, M., Smith, P., Wegryn, E., 1999. Properties of dust in the martian atmosphere from the Imager on Mars Pathfinder, Journal of Geophysical Research 104, Issue E4, 8987-9008

Veefkind, J.P., 1999. Aerosol Satellite Remote Sensing, PhD thesis, ISBN 90-393-2173-6. Also available at: http://www.knmi.nl/~veefkind/documents/PhDThesisPepijnVeefkind.pdf

Wolff, M.J., Smith, M.D., Clancy, R.T., Spanovich, N., Whitney, B.A., Lemmon, M.T., Bandfield, J.L., Banfield, D., Ghosh, A., Landis, G., Christensen, P.R., Bell, J.F., Squyres, S.W., 2006. Constraints on dust aerosols from the Mars Exploration Rovers using MGS overflights and Mini-TES, Journal of Geophysical Research, Volume 111, Issue E12, CiteID E12S17

Zasova, L., Formisano, V., Moroz, V., Grassi, D., Ignatiev, N., Giuranna, M., Hansen, G., Blecka, M., Ekonomov, A., Lellouch, E., Fonti, S., Grigoriev, A., Hirsch, H., Khatuntsev, I., Mattana, A., Matutilli, A., Moshkin, B, Patsaev, D., Piccioni, G., Rataj, M., Saggin, B., 2005. Water clouds and dust aerosols observations with PFS MEX at Mars. Planetary and Space Sciences 53, Issue 10, pp. 1065-1077

ACCEPTED MANUSCRIPT

HRSC image numbers	h4165_0000
Observation date	April 3, 2007
Panchromatic	585—765 nm
Solar inc. angle S1 # P1 # ND # P2 # S2	(16:20—16:30 h local time) 64.8° # 64.8° # 64.7° # 64.6° # 64.5°
Emission angle S1 # P1 # ND # P2 # S2	20.3°-20.4° # 13.5°-13.6° # 1.4°-1.5° # 14.3°-14.4° # 21.0°-21.2°
Phase angle S1 # P1 # ND # P2 # S2	67.8°-68.4° # 66.0°-66.6° # 63.4°-64.0° # 62.4°-63.0° # 62.6°-63.2°
Solar longitude	231° (mid southern spring)

Table 1. Information on the HRSC images of Gusev crater that were used to measure the correction factor C. The given observation geometry is for the region with the analyzed shadowed and sunlit comparison regions.

HiRISE image number	TRA_0873_1780
Observation date	October 3, 2006
Near Infra Red	800—1000 nm
Red	550—850 nm
Blue-green	400—600 nm
Solar incidence angle	56.2° (15.445 h local time)
Emission angle	3.8°
Phase angle	59.3°
Solar longitude L_s	115.34 (northern summer)

Table 2. Information on the analyzed HiRISE images.

	τ_{S1}	τ_{P1}	τ_{nd}	τ_{P2}	τ_{S2}	altitude
Region 0 ➔ @ altitude Spirit	0.52 **0.56**	0.51 **0.55**	0.51 **0.55**	0.52 **0.56**	0.52 **0.56**	-2693 m -3670 m
Region 1 ➔ @ altitude Spirit	0.54 **0.59**	0.54 **0.59**	0.54 **0.59**	0.54 **0.59**	0.55 **0.60**	-2657 m -3670 m
Region 2 ➔ @ altitude Spirit	0.50 **0.51**	0.50 **0.51**	0.49 **0.50**	0.50 **0.51**	0.50 **0.51**	-3447 m -3670 m
Region 3 ➔ @ altitude Spirit	0.52 **0.53**	0.51 **0.52**	0.49 **0.50**	0.49 **0.50**	0.50 **0.51**	-3450 m -3670 m
Region 4 ➔ @ altitude Spirit	0.54 **0.55**	0.53 **0.54**	0.52 **0.53**	0.51 **0.52**	0.51 **0.52**	-3467 m -3670 m
$<\tau_{shad}>$ translated to Spirit's altitude	**0.55** ± 0.03	**0.54** ± 0.03	**0.53** ± 0.04	**0.54** ± 0.04	**0.54** ± 0.04	-3670 m
τ_{sp}	0.76 ± 0.03					-3670 m
$C = <\tau_{shad}>/ \tau_{sp}$	0.72 ± 0.04	0.71 ± 0.04	0.70 ± 0.05	0.71 ± 0.05	0.71 ± 0.05	
Average correction factor **C = 0.71 ± 0.06**						

Table 3. Shadow method retrievals from 5 regions, shown in the upper panel of Figure 6, in the rim of Gusev crater. Section 5.2 elaborates about the error of ± 0.06 that is assigned to the correction factor C. Details about the analyzed images are given in Table 1, and Section 4.2, and the results are discussed in Section 5.2. The shadow method estimates τ_{S1shad}, τ_{P1shad}, τ_{ndshad}, τ_{P2shad}, and τ_{S2shad} are retrieved from the imagery taken by the

sensors S1, P1 nd, P2, and S2 respectively and are printed in the upper part of the cells for regions 0—4; the numbers printed in bold below these in the same cells are the values that presumably would have been measured if the analyzed regions were at the same altitude as the Spirit rover and if the scale-height of optical depth was about 12 km. The column “altitude” gives the average altitude of the sunlit comparison regions (upper value), and the altitude of Spirit. The rows below those for regions 0—4 are: the average optical depth $\langle\tau_{shad}\rangle$ translated to the altitude of Spirit, the optical depth τ_{sp} that was measured by Spirit, and the correction factors (explained in e.g., Section 5.1).

Figure 1. Part of the HRSC nadir image taken during orbit 1944. It covers the regions that were analyzed in Valles Marineris. North is up. Black lines denote analyzed sunlit pixels and white ones analyzed pixels in shadow. Each black line is paired to a nearby white one and each pair was used for a shadow method estimate of the optical depth τ_{shad}. See Section 3 for details. We used the full set of nine stereo and color ortho-images and retrieved more than 150 τ_{shad} from each image, using the same locations of shadow and sunlit comparison regions for all nine images. For clarity, we indicate a sample of only 20 of these retrievals. The τ_{shad} that were retrieved for this sample are: **1** 0.41 ± 0.07 **2** 0.41 ± 0.05 **3** 0.58 ± 0.06 **4** 0.31 ± 0.03 **5** 0.54 ± 0.06 **6** 0.52 ± 0.04 **7** 0.44 ± 0.04 **8** 0.43 ± 0.03 **9** 0.26 ± 0.02 **10** 0.33 ± 0.01 **11** 0.48 ± 0.05 **12** 0.26 ± 0.01 **13** 0.28 ± 0.01 **14** 0.41 ± 0.02 **15** 0.46 ± 0.03 **16** 0.38 ± 0.01 **17** 0.32 ± 0.03 **18** 0.41 ± 0.03 **19** 0.39 ± 0.01 **20** 0.33 ± 0.02

Figure 2. Altitude versus shadow method estimates τ_{shad} for the about 150 regions that were analyzed in each of the five panchromatic images. The smooth curves are fits. See Section 5.3 for details. The lower right hand panel shows these fits for the five images together in one plot; going from top to bottom the curves are for: S1, P1, S2, P2, and nd. Each fit is used to calculate a scale-height and S1, P1, S2, and P2 yielded values between 12 and 13 km. The spread between these probably reflects a mix of measurement noise and phase-angle effects. The fit on the retrievals from the nadir image yielded only 11.3 km.

ACCEPTED MANUSCRIPT

Figure 3. Similar to Figure 2 but for shadow method estimates τ_{shad} from the four color images and the nadir one. In the lower right hand panel the five fits have been plotted into one panel; going from top to bottom at an altitude of around 3 km, the curves are for: blue, green, NIR, red, and nd. For blue and green the retrieved optical depths and scale-heights are clearly larger than for the other images. The optical depths that are derived from the NIR image are, relative to those derived from the other ones, low at high altitudes and high at low altitudes. We speculate that this is a result of a decreasing average aerosol size with altitude. See Section 5.1.4 for discussion.

Figure 4. Optical depth as a function of wavelength at 5 different altitudes. Going from top to bottom the altitudes are: 0.87 km, 2.12 km; 4.9 km; 6.62 km, 8.25 km. At the highest altitude, the optical depths from the blue image are more than 30% larger than those from the panchromatic ones, but at lower altitudes the difference is much smaller. There is no significant difference in the retrieved optical depths between the panchromatic and red images. For lower altitudes it is slightly larger in NIR than in red.

Figure 5. All nine HRSC images from orbit 1944 yielded an estimate of the scale-height of optical depth in Valles Marineris. These scale-heights are plotted as a function of color. The five panchromatic images are all observed in the same wavelength range around 675 nm; from the lowest to the highest scale-heights that are retrieved from these panchromatic images the results are for: nadir, P2, S2, S1 and P1 (P1 and S1 are close to identical). The phase-angles range between 65° and 80°. The retrieved scale-heights clearly increase from NIR towards the blue. See Section 5.1.4 for discussion.

Figure 6. A fragment of a HRSC nadir image from orbit 4165 of MEX. South is to the left. The width of the image is about 48 km. It shows the rim of Gusev crater, and the locations that were used for the shadow method retrievals. The region is around 100 km southwards of the landing site of the Spirit rover (not visible in the image) that measured a ground truth of $\tau_{sp} = 0.76 \pm 0.03$ on that Sol. We correct for slight altitude differences between the regions (see Section 5.2). **Numbers:** the sunlit comparison regions are close to the shadows and the retrieved τ_{shad} all range between 0.49 and 0.55 (see Table 3). S1, P1, P2, and S2 yielded values that typically were 0.01-0.02 higher than those for the nadir image. Dividing the shadow method retrievals by a correction factor $C \approx 0.71$ yields the atmospheric optical depth with an accuracy of maybe $\pm 8\%$. **Letters:** the sunlit comparison regions are far away from the shadows and the shadow method yields much lower estimates. In the nadir image A and B yielded 0.38 and C and D yielded 0.40, with an average of $\tau_{shad} = 0.39 \pm 0.01$. For the other images, the average and all individual retrieved values are 0.01-0.02 higher. Choosing the sunlit comparison regions at large distances from the shadows leads to smaller correction factors. In this case it is $C \approx 0.54$. The shadow method estimates and resultant correction factors increase gradually when moving the sunlit comparison regions towards the mountains that cast the shadows and reach $C \approx 0.71$ when close to the shadows.

Figure 7. Victoria crater in a HiRISE red image. The diameter of the crater is about 750 meter and it is up to 70 meters deep. White: analyzed regions in shadow. Black: sunlit comparison regions. The sunlit comparison regions denoted by numbers are located in the almost flat central part of the crater (see Section 5.3.2 for details). The τ_{shad} that were retrieved for these are: **1** 0.34 ± 0.08, **2** 0.33 ± 0.08, **3** 0.34 ± 0.09, **4** 0.33 ± 0.08, **5** 0.31 ± 0.07, **6** 0.33 ± 0.07, **7** 0.31 ± 0.06, **8** 0.34 ± 0.07, **9** 0.32 ± 0.05, **10** 0.33 ± 0.06, **11** 0.33 ± 0.02, **12** 0.31 ± 0.05, **13** 0.30 ± 0.04, **14** 0.28 ± 0.01, **15** 0.31 ± 0.03, **16** 0.33 ± 0.06, **17** 0.33 ± 0.06, **18** 0.34 ± 0.05, **19** 0.34 ± 0.05, **20** 0.32 ± 0.04. The sunlit comparison regions denoted by letters are on a slope that is tilted towards the sun (see Section 5.3.3 for details). For these, the retrieved τ_{shad} are: **A** 0.30 ± 0.02, **B** 0.29 ± 0.02, **C** 0.28 ± 0.03, **D** 0.28 ± 0.03, **E** 0.28 ± 0.03, **F** 0.28 ± 0.03

Figure 8. Detail of Figure 7. A shadowed region in the Northern part of Victoria crater and sunlit comparison regions of varying albedo. The retrieved τ_{shad} are: **A** 0.46 ± 0.02, **B** 0.45 ± 0.02, **C** 0.33 ± 0.03, **D** 0.32 ± 0.02, **E** 0.27 ± 0.03, **F** 0.27 ± 0.03, **G** 0.65 ± 0.07, **H** 0.63 ± 0.06, **I** 0.47 ± 0.03, **J** 0.46 ± 0.02. See Section 5.3.3 for discussion.

ACCEPTED MANUSCRIPT

1230 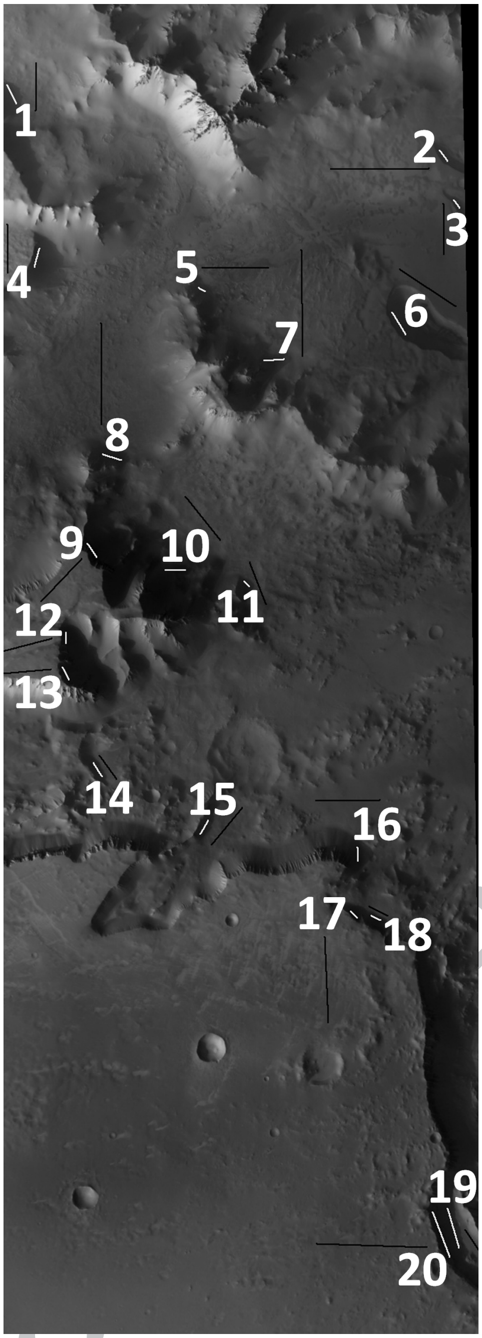

1231 Figure 1.

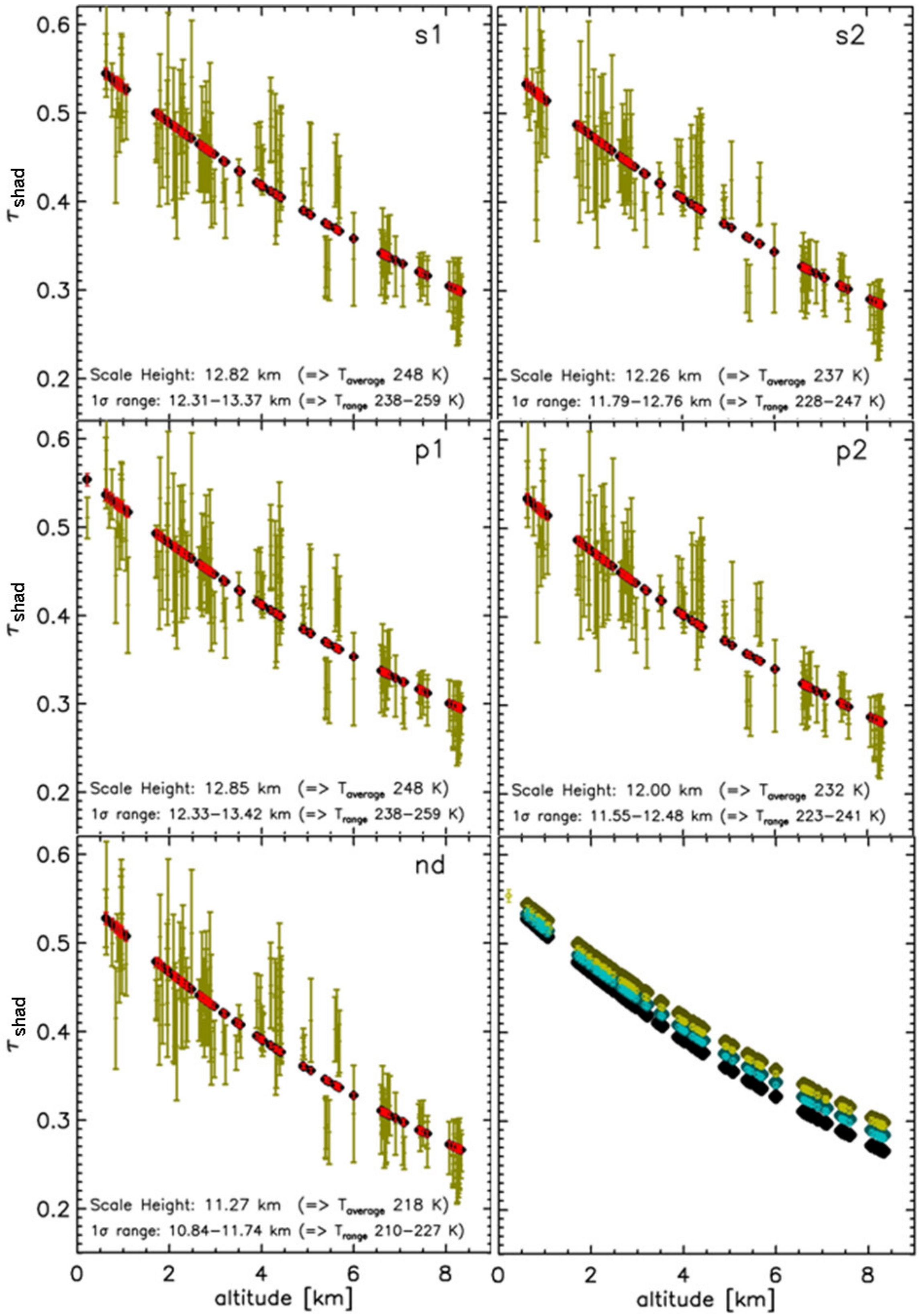
s1
Scale Height: 12.82 km (=> $T_{average}$ 248 K)
1σ range: 12.31–13.37 km (=> T_{range} 238–259 K)
s2
Scale Height: 12.26 km (=> $T_{average}$ 237 K)
1σ range: 11.79–12.76 km (=> T_{range} 228–247 K)
p1
Scale Height: 12.85 km (=> $T_{average}$ 248 K)
1σ range: 12.33–13.42 km (=> T_{range} 238–259 K)
p2
Scale Height: 12.00 km (=> $T_{average}$ 232 K)
1σ range: 11.55–12.48 km (=> T_{range} 223–241 K)
nd
Scale Height: 11.27 km (=> $T_{average}$ 218 K)
1σ range: 10.84–11.74 km (=> T_{range} 210–227 K)
τ_{shad}
altitude [km]

Figure 2.

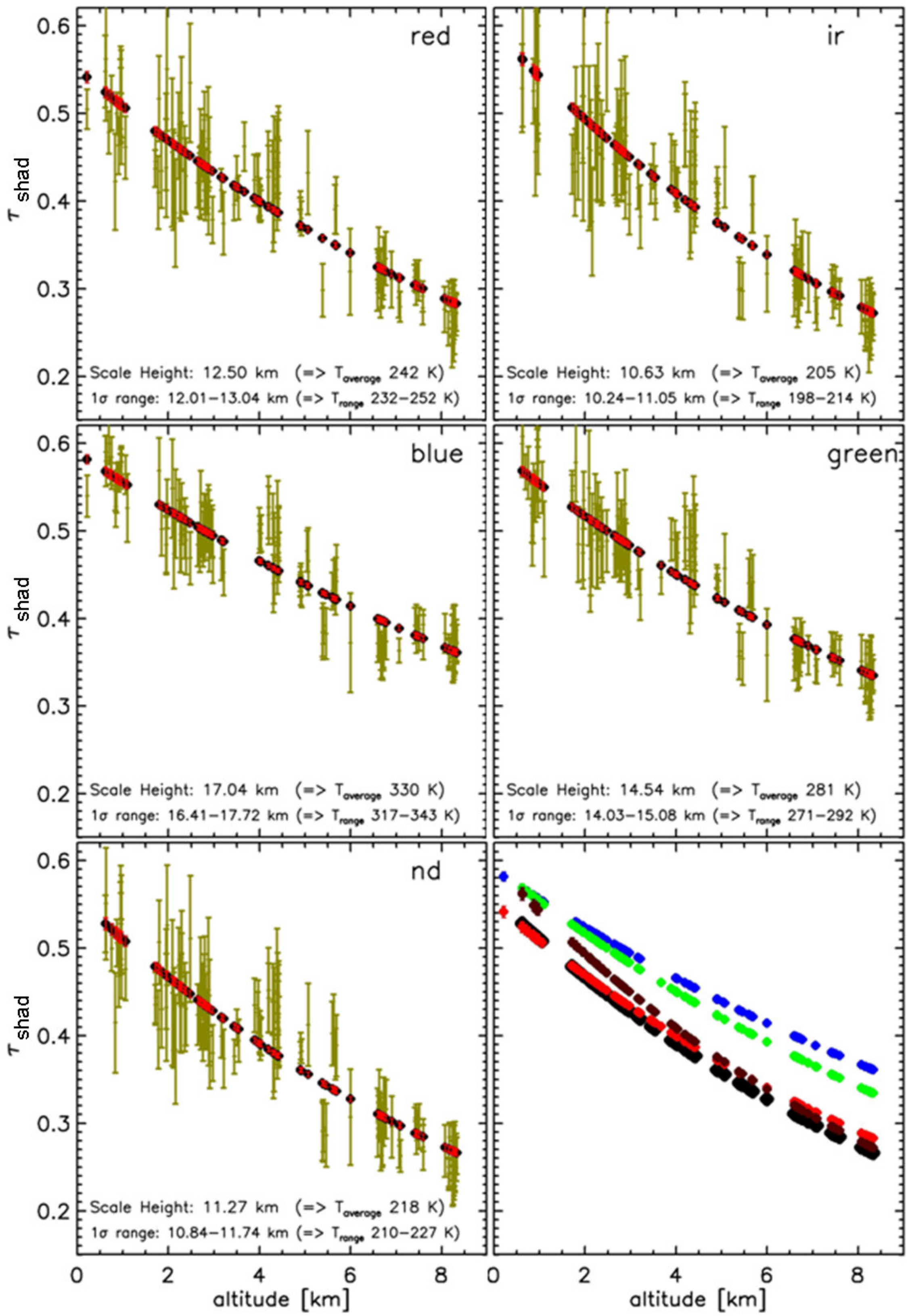

1234

1235 Figure 3.

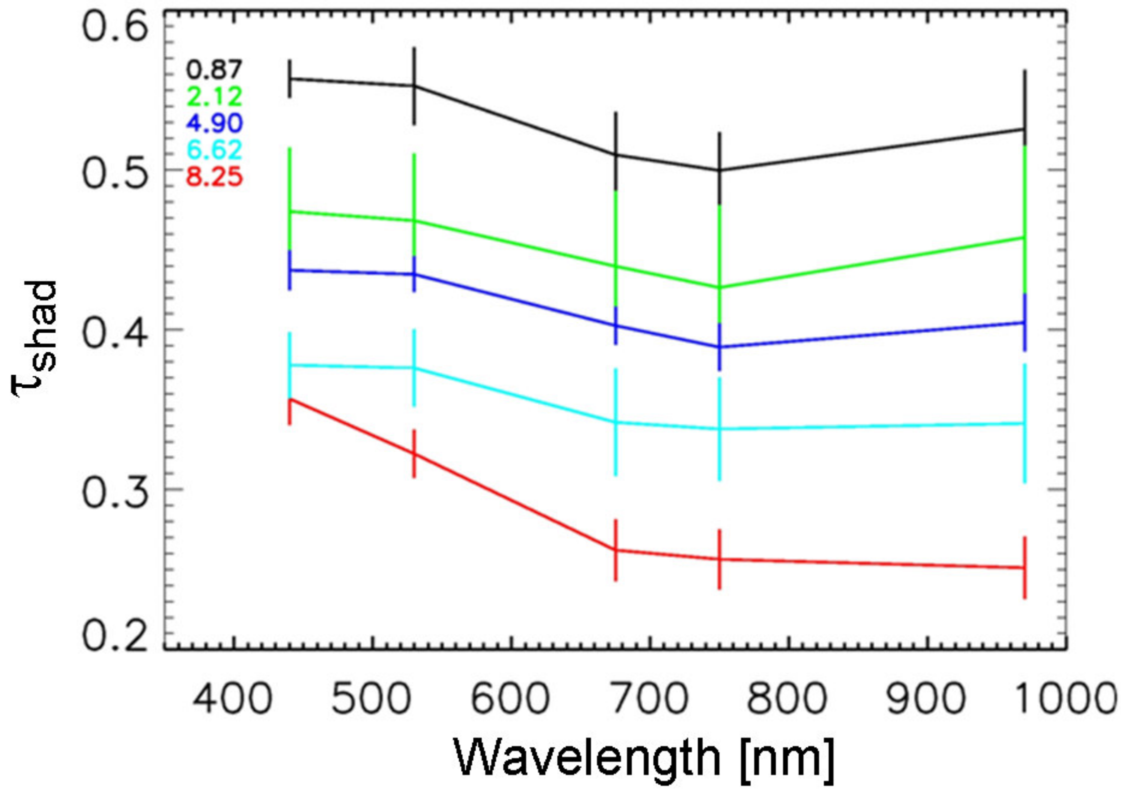

1236

1237 Figure 4.

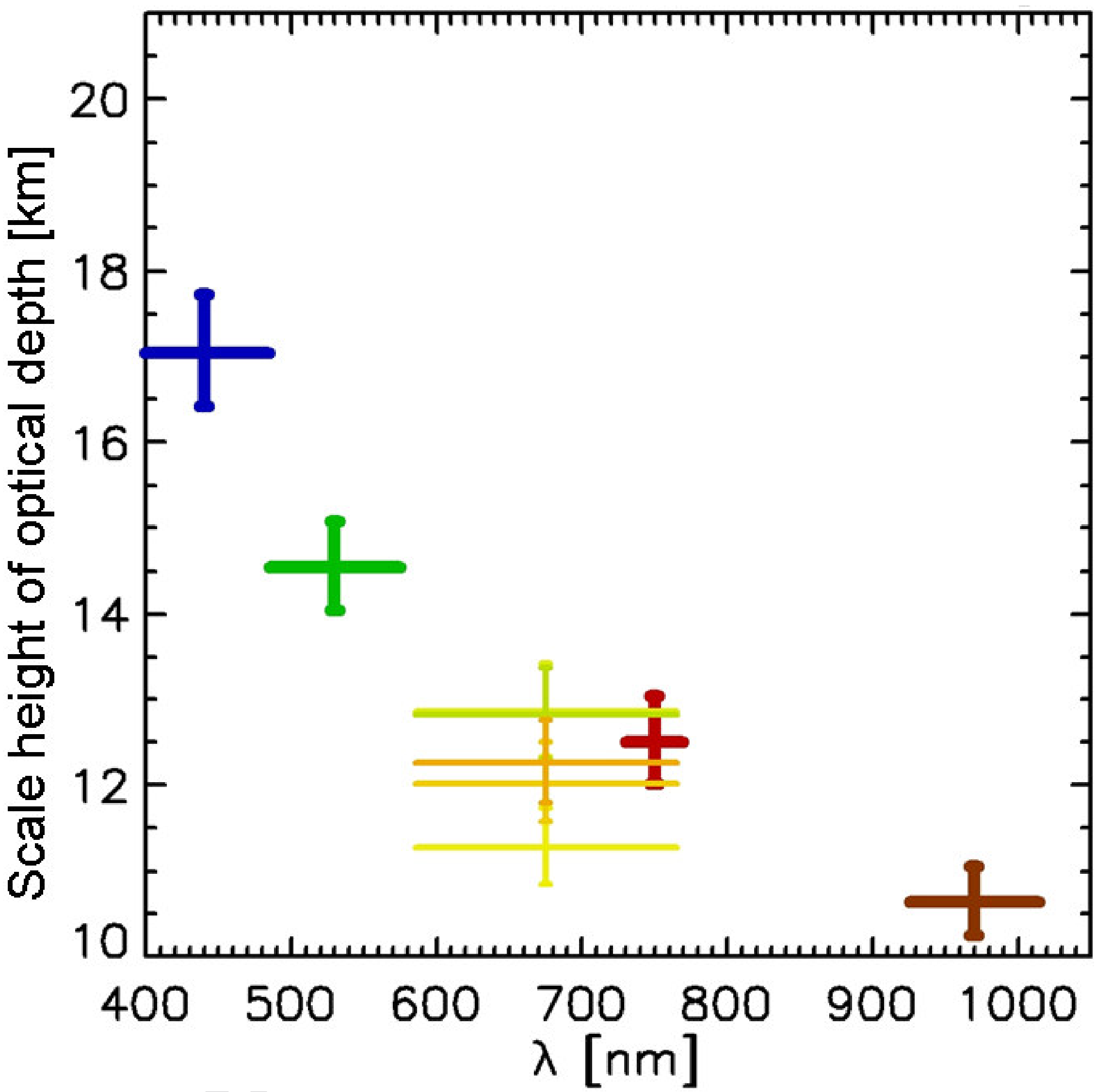

1238

1239 Figure 5.

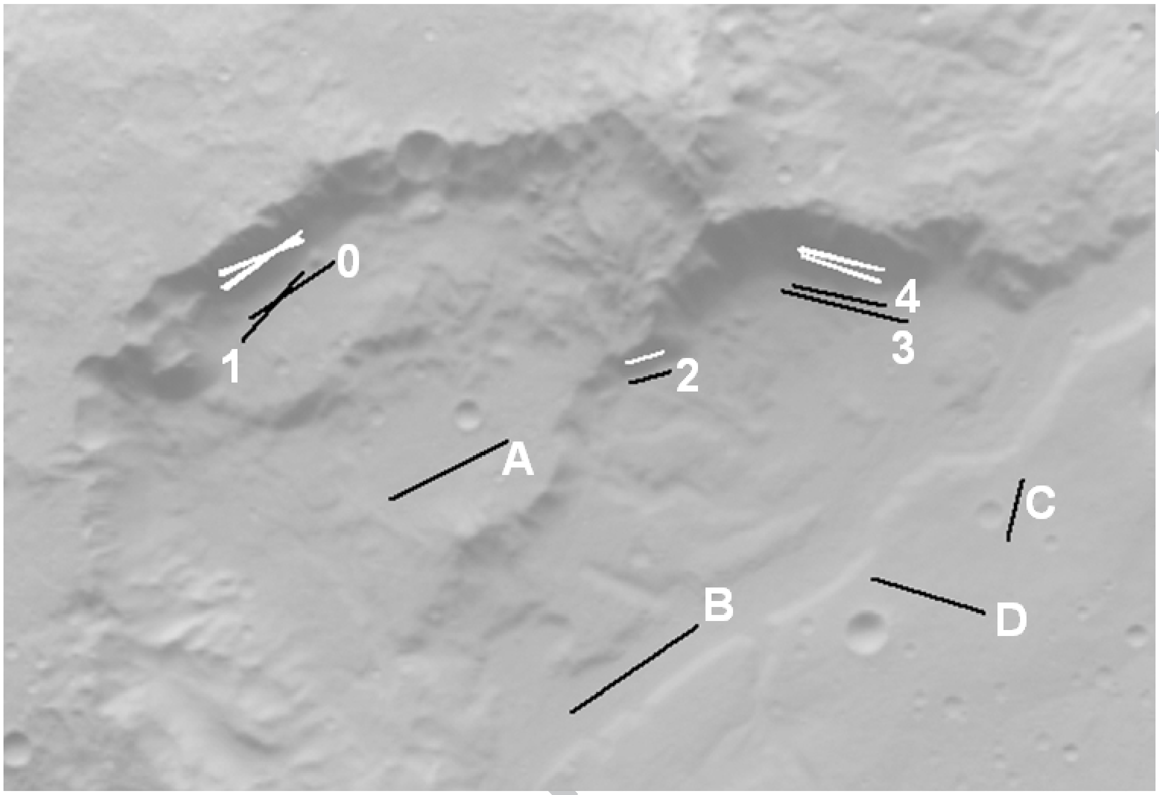

Figure 6.

1243

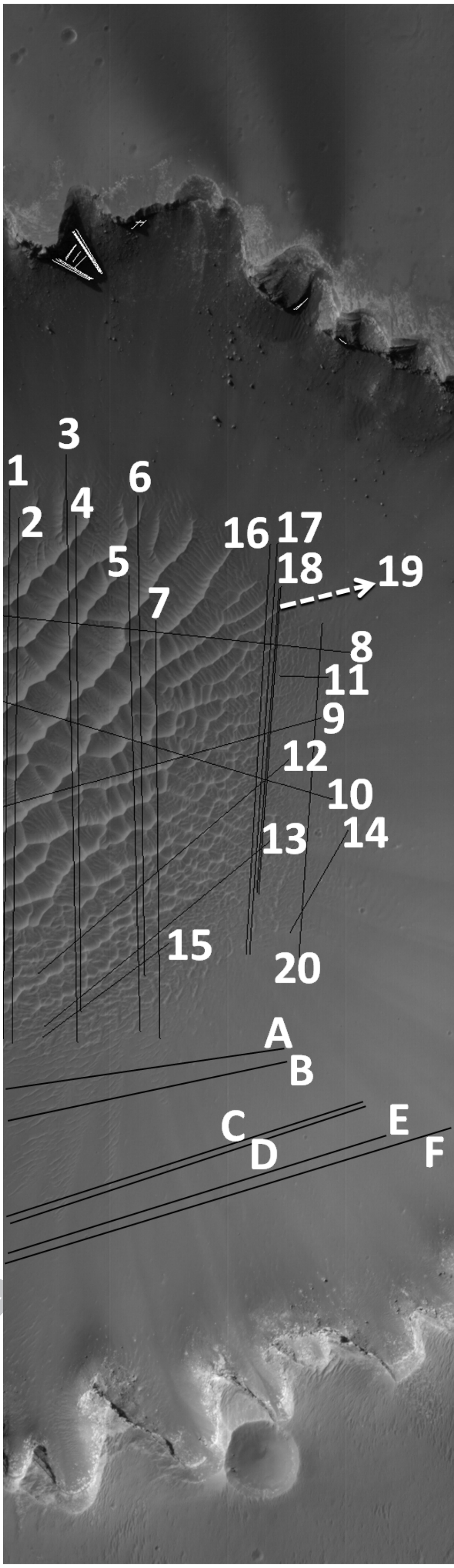

Figure 7.

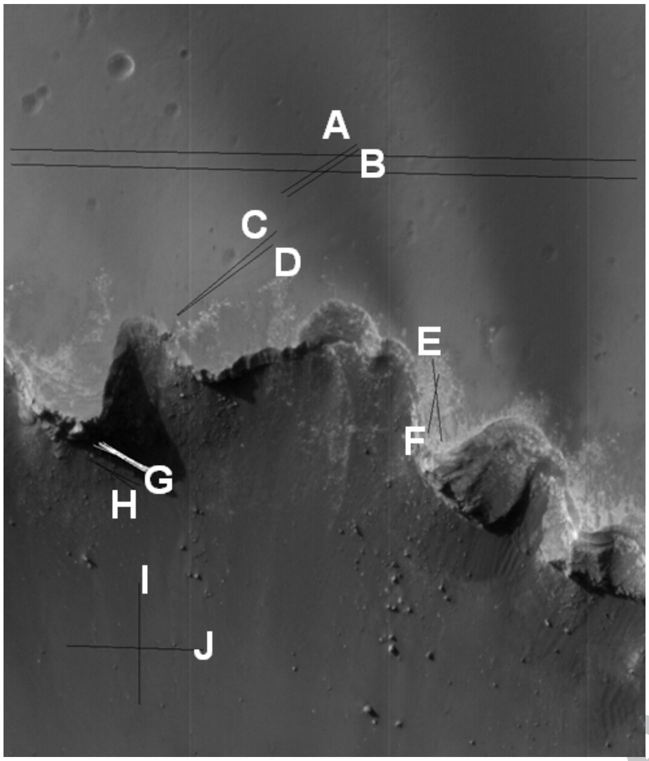

Figure 8.

>The optical depth of the Martian atmosphere determines the brightness of shadows
>We estimate the optical depth from the brightness of shadows in orbiter images
>It is best to use images taken in colors between yellow and red
>Two case studies suggest an accuracy of ±15% or better between yellow and red